

# Landslide Spreading, Impulse Water Waves and Modelling of the Vajont Rockslide

Giovanni B. Crosta<sup>1</sup> · Silvia Imposimato<sup>2</sup> · Dennis Roddeman<sup>2</sup>

Received: 30 September 2014 / Accepted: 8 May 2015 / Published online: 27 May 2015  
© Springer-Verlag Wien 2015

**Abstract** Landslides can occur in different environments and can interact with or fall into water reservoirs or open sea with different characteristics. The subaerial evolution and the transition from subaerial to subaqueous conditions can strongly control the landslide evolution and the generated impulse waves, and consequently the final hazard zonation. We intend to model the landslide spreading, the impact with the water surface and the generation of the impulse wave under different 2D and 3D conditions and settings. We verify the capabilities of a fully 2D and 3D FEM ALE approach to model and analyse near-field evolution. To this aim we validate the code against 2D laboratory experiments for different Froude number conditions ( $Fr = 1.4, 3.2$ ). Then the Vajont rockslide ( $Fr = 0.26–0.75$ ) and the consequent impulse wave are simulated in 2D and 3D. The sliding mass is simulated as an elasto-plastic Mohr–Coulomb material and the lake water as a fully inviscid low compressibility fluid. The rockslide model is validated against field observations, including the total duration, the profile and internal geometry of the final deposit, the maximum water run-up on the opposite valley flank and on the rockslide mass. 2D models are presented for both the case of a dry valley and that of the impounded lake. The set of fully 3D simulations are the first ones available and considering the rockslide evolution, propagation and interaction with the water reservoir. Advantages and disadvantages of the modelling approach are discussed.

**Keywords** Vajont rockslide · Impulse wave · Tsunami · Coupled modelling · Fully 3D FEM ALE · Elasto-plastic Mohr–Coulomb · Landslide–reservoir interaction

## 1 Introduction

Natural or artificial valley damming and consequent water impounding can cause the reactivation of slope instabilities along the directly affected valley sides. In other cases the interaction of landslides with natural and artificial lakes or fjords and open sea can occur because of their long runout along the slopes. Debris flows are characterized by long runout, but commonly relatively limited volumes and velocity. Then their consequences in terms of generated water waves within the water reservoir are generally limited. On the contrary, large rockslides, rock and debris avalanches involve large to extremely large volumes (millions to hundred of millions of cubic metres), can reach extremely high speed along subaerial slopes (tens of metres per second) and the impact can involve a variably steep landslide snout and an immobile mass of water. The moving masses can be characterized by completely different properties, ranging from coarse to fine granular materials up to more or less fractured and open rock masses. Therefore, the spreading of large landslide masses can originate large waves with characters controlled by many different factors, such as: the landslide initial position (e.g. high on a slope, partially submerged or completely submerged), the landslide speed, the type of material, the slope inclination and its geometry, both subaerial and subaqueous, the relative size of the landslide mass with respect to the depth of water, the soil and rock mass properties and stiffness contrast. Historical observations demonstrate that these phenomena are highly destructive, even if associated with

---

✉ Giovanni B. Crosta  
giovannibattista.crosta@unimib.it

<sup>1</sup> Dipartimento di Scienze Geologiche e Geotecnologie,  
Università degli Studi di Milano-Bicocca, Milan, Italy

<sup>2</sup> FEAT, Maaierhof 27, 6418 JL Heerlen, The Netherlands

relatively small volumes, and can be characterised by a high recurrence frequency at sites susceptible to landsliding.

Extreme landslide tsunami or impulse wave events occurred as a consequence of subaerial landslides at very different sites in recent historical times. In Norway, rock-fall and rock avalanches and the associated tsunamis (Jørstad 1968) represent an extremely serious natural hazard which in the last 400 years claimed the lives of about 250 (Harbitz et al. 2014) in four main events (1934 Tafjord rockslide-fall,  $1.5$  to  $3 \times 10^6$  m<sup>3</sup>, Blikra et al. 2005; Mt. Ramnefjellet on 15 January 1905,  $0.35 \times 10^6$  m<sup>3</sup> and 13 September 1936,  $1 \times 10^6$  m<sup>3</sup>; 1756 Langfjord rockslide,  $12 \times 10^6$  m<sup>3</sup>).

The Lituya Bay (Alaska, Miller 1960) has been a site of multiple historical slope failures and tsunamis, with recorded events in 1853–1854, 1936 and 1958. The famous July 9, 1958 event occurred as a consequence of a  $30 \times 10^6$  m<sup>3</sup> rock avalanche, triggered by 8.3  $M_w$  and resulted in an impulse wave with exceptional wave run-up (about 524 m) and waves between 30 and 90 m along the Lituya Bay and claimed five victims. Slingerland and Voight (1979) describe the 1792 Shimabara Bay (Japan) complex slide ( $535 \times 10^6$  m<sup>3</sup>) which moved into the sea along a 4.8-km front, generating 10-m-high waves and claiming 15,000 lives. The small 1971 Chungar collapse (Perù,  $0.1 \times 10^6$  m<sup>3</sup>) in the Yanahuin Lake caused a 30-m-high water wave run-up and the loss of 400–600 lives (Plafker and Eyzaguirre 1979).

On 22 March 1959, a  $3 \times 10^6$  m<sup>3</sup> rock and debris slump rapidly moved within the Pontesei artificial water reservoir, when water depth was about 47 m, during a rapid reservoir level drawdown (Catenacci 1992; Semenza 2002; Panizzo et al. 2005b). The landslide displacement (ca 120 m) lasted 2–3 min (i.e. velocity between 0.7 and 1 m s<sup>-1</sup>) with a 33-m-high water wave passing the dam of 20-m height and caused one casualty. The event occurred just during the construction of the Vajont dam and led to the beginning of the studies of the Vajont reservoir slope stability (Semenza 2010).

The 1963 Vajont rockslide (Italy, about 2000 casualties), which will be described in the following, was characterized by an extremely low water depth to landslide thickness ratio. Similar conditions occurred also with the 1987 Val Pola rock avalanche (July 28th; Crosta et al. 2003) which evolved downslope as a coarse granular mass and impacted on a shallow debris dammed lake generating a wave of muddy water and rock avalanche debris which propagated up to 2.7 km upstream, destroying three villages and killing 27 persons.

Finally, some major events are associated with catastrophic collapses of volcanic islands and edifices in deep ocean waters (Hawaii and Canary islands, Keating and

McGuire 2000; Ward and Day 2003) or water reservoirs (e.g. Spirit Lake at the Mt St Helens collapse, 1980, and shallow lakes, Sosio et al. 2012) and glacier collapse (e.g. Disenchantment Bay, Alaska, 1850, 1905; Slingerland and Voight 1979).

Many other events are associated with subaqueous landslides of very different sizes and triggering, but this type of phenomena are not directly considered in this paper. Presently, this type of extreme risk has been recognized at many sites around the world, among which are the Usoi–Sarez Lake (Tajikistan, Pamir, Ischuk 2011), Laxiwa water reservoir, Three Gorges Lake (China, Zhang et al. 2013), Yangtze Three Gorges Lake (Wang et al. 2005; Wang and Li 2009) and Aknes rock slope (Western Norway, Blikra et al. 2006).

The Usoi–Sarez Lake ( $17 \times 10^9$  m<sup>3</sup>) was formed by a  $2.2 \times 10^9$  m<sup>3</sup> rock avalanche which dammed the Murgab River (Ischuk 2011) after the M 7.4 earthquake on February 18, 1911. The valley flanks along the lake are characterized by the presence of very large rockslides (up to  $0.9 \times 10^9$  m<sup>3</sup>) which could generate large water waves in case of rapid collapse and the consequent overtopping and rapid erosion of the Usoi rock avalanche landslide dam.

The construction of the 4200-MW Laxiwa hydropower station (Zhang et al. 2013), located along the main reach of the upper Yellow River (China), started in 2001, and the lake ( $1.08 \times 10^9$  m<sup>3</sup>) impoundment began in 2009. Since then, the right hand slope in granitic rock, just 0.5 km upstream of the 250-m-high concrete double-curvature arch dam, started moving along a 1-km-long and 0.7-km-high front (ca.  $70 \times 10^6$  m<sup>3</sup>). Zhang et al. (2013) show that total displacements along the upper scarp reached 26 m on October 2010, and large deformations were recorded at depth within the rockslide mass.

The Yangtze Three Gorges project (Wang et al. 2005; Wang and Li 2009) generated a 660-km-long lake, which triggered an estimated total number of about 5386 landslides. 392 landslides were characterized by a volume larger than  $0.01 \times 10^6$  m<sup>3</sup> (Wang and Li 2009), of which 74 were with volume larger than  $1 \times 10^6$  m<sup>3</sup>. Some of them have a potential for generating water waves, such as the Qianjinangping landslide (ca.  $20 \times 10^6$  m<sup>3</sup>; Wang et al. 2005) which claimed 24 lives, of which 11 was because of the water wave reaching an estimated height of about 30 m.

The Åkerneset rockslide (ca  $54 \times 10^6$  m<sup>3</sup>) is located along the fjord Sunnylvsfjorden (Storfjorden, Møre & Romsdal County) in Western Norway not far from the Tafjord rockslide. Blikra et al. (2006) recognized at least 12 large rockslides in the inner Storfjorden area that occurred in the last 400 years causing a total of 68 tsunami fatalities. Because of the increased population and of the touristic presence, it is expected that the potential risk is

now much larger than in the past. In fact, the Geirangerfjord, just a few kilometres from the Åkerneset site, is visited annually by about 700 000 tourists on 150–200 cruise ships. Harbitz et al. (2014) computed the expected tsunami waves at different locations along the fjord for different rockslide scenarios resulting, for example, in maximum run-up heights of 70 and 85 m at Geiranger and Hellesylt, respectively.

Since the 1963 Vajont event, a large number of landslides along water reservoir shorelines are under continuous monitoring, investigation and stabilization to verify or eliminate the possible transition from a slow- to a fast-moving landslide (e.g. Macfarlane 2009; Kalenchuk et al. 2012; Zangerl et al. 2010; Barla et al. 2010). At the same time, most of the national agencies and companies in charge of the construction, management and control of hydroelectric power plants defined specific guidelines for the safety of the hydropower dams in relation to impulse water waves associated with mass movements (e.g. rockslides and rock avalanches, rock falls, debris flows, snow avalanches), both concerning the endangered areas and the effects on the dam structures. These standards and guidelines have also been the main reason for developing a conspicuous set of experimental tests and numerical models through the last decades (Harbitz et al. 2014).

### 1.1 Rockslides and Impulse Waves

Rock slides (Varnes 1978, Cruden and Varnes 1996) are landslides which imply a mass or a contiguous group of prevalently bedrock masses that moved or is moving along a major failure surface (planar or curved), or on relatively thin zones of intense shear strain. The displaced mass may appear as a single intact block (i.e. blockslide) or may be disrupted, with evidence of some distributed deformation, varying both in time and space within the slide. For very large rapid displacements and degree of disruption and fragmentation, the rockslide can transform into a rock avalanche.

Landslide-generated impulse waves (i.e. landslide tsunamis; Slingerland and Voight 1979) can be subdivided into three different evolutionary steps: initiation, propagation and, finally, run-up. They are generally characterized by larger heights in the near field, by rapid decay, high turbulence, flow separation and subsequent reattachment, and strong mixing of air and water.

Erismann and Abele (2001) suggest a three-phase evolution for water reservoirs affected by the rapid movement of rockslides with settings similar to the Vajont rockslide. During the first phase, the wedge-shaped rockslide front exerts both a lifting and accelerating force on the water, decreasing with the differential velocity between the two

masses. The water mass gets thinner by longitudinal and/or lateral spreading and this phase ends in a momentary standstill of the water with respect to the slope. In the second phase, water starts flowing back, acquiring a velocity increasingly larger than that of the rock mass and reaching the maximum when passing the distal edge of the rockslide. Finally, once past the rockslide toe, the water moves under its own kinetic energy and the run-up height is roughly proportional to the square of the velocity at the beginning of the run-up.

On the other hand, both the evolution of the rockslide and of the water impulse wave can be controlled by the resistance to motion and the permeability of the rock or debris mass. This point is extremely interesting and has been partially tackled by Zhao et al. (this issue) where the mechanical upscaling of the particle size allows for a reasonable computation time, allowing to partially control the effects of a very high permeability of the simulated rock mass. As shown by Zhao et al. (this issue), the high permeability partially neutralizes the rockslide thrust on the water mass allowing for a rapid filtration of the reservoir water into the rockslide mass.

Erismann and Abele (2001) discuss three different scenarios of varying the permeability of the rock mass, inducing a different hydrodynamic resistance. If permeability is extremely large, most if not all of the water volume can be sorbed within the rockslide, dissipating energy by water filtration through the mass. Anyway, the authors neglect completely the fact that generally groundwater is already saturating most of the rockslide mass below the reservoir water level. In case of a very compact or low permeability rock/debris mass, considering the very rapid evolution of a rockslide–rock avalanche, this will behave as an impermeable mass allowing run-up both on the landslide mass and subsequently on the opposite valley flank controlled by the rockslide profile and superficial characteristics. Intermediate conditions are possible and will be controlled by the permeability and type of openings (i.e. fractures, more or less interconnected, pores). Again, the presence of groundwater saturating part of the rockslide mass and seeping through it can strongly influence the filtration of the reservoir water within the mass.

Laboratory experiments considering the effects of landslides on the generation of impulse waves have been performed since a long time and using different approaches (e.g. vertically falling boxes with different block height to water depth ratios; Wiegel et al. 1970; Noda 1970; sliding rigid boxes, Wiegel et al. 1970; Watts 1998, 2000; Panizzo et al. 2005a; Sue et al. 2006; Enet and Grilli 2007; Ataie-Ashtiani and Nik-Khah 2008; Sælevik et al. 2009; sand bags, Davidson and McCartney 1975; granular masses, Huber 1980, 1982; Fritz et al. 2003a, b, 2004, 2009; Heller and Hager 2010, Heller 2007) and a useful summary of

these techniques and findings is presented by Di Risio et al. (2011).

Then, results from various systematic experimental works on 2D and 3D wave generation and propagation (Kamphuis and Bowering 1970; Huber 1980; Müller 1995; Huber and Hager 1997; Fritz 2002; Zweifel 2004; Panizzo et al. 2005a, b; Heller 2007; Heller and Kinnear 2010; Sælevik et al. 2009), using both rigid blocks and deformable granular masses, can be used to calibrate and validate numerical modelling tools. These experiments have shown that rigid boxes generate larger waves than in case of deformable masses.

Analytical (Noda 1970), empirical (Slingerland and Voight 1979; Ataie-Ashtiani and Malek-Mohammadi 2007) and numerical methods (Quecedo et al. 2004; Abadie et al. 2010) have been developed and applied to simulate landslide-induced tsunamis. In most of these studies, the subaerial movement has been analysed in a simplified way (Noda 1970; Harbitz 1992; Jiang and LeBlond 1993; Grilli et al. 2002; Grilli and Watts 2005; Lynett and Liu 2005; Abadie et al. 2010) and simplified rheologies (e.g. viscous rheologies) have been considered for subaqueous spreading.

In this paper, we focus our attention on the simulation of the initiation or generation of impulse waves by the rapid movement and impact of a landslide mass. In particular, we are interested in the simulation of a landslide mass, considered as a continuous deformable material, spreading along a slope of variable geometry, both under subaerial and submerged conditions, and its interaction with the water body. To validate our FEM ALE numerical approach, we simulate some 2D experimental tests performed by Fritz (2002) and Sælevik et al. (2009) considering deformable masses and rigid blocks, respectively. Then, we present both the 2D simulation along a well-documented Vajont rockslide cross section and the 3D simulation of the Vajont rockslide and of the generated impulse wave. The results are compared with real observations, estimates from other authors and with results from DEM modelling presented by Zhao et al. (this issue).

## 1.2 Vajont Rockslide

The October 9, 1963 Vajont landslide (Semenza 1965, Semenza and Ghirotti 2000; Ghirotti 2012) has been studied frequently (e.g. Broili 1967; Ciabatti 1964; Semenza and Ghirotti 2000; Hendron and Patton 1985; Müller 1964; Sitar et al. 2005; Vardoulakis 2000; Veveakis et al. 2007; Alonso and Pinyol 2010; Pinyol and Alonso 2010; Alonso et al. 2010; Boon et al. 2014) because of its nature, the catastrophic consequences and the unexpected effects, and the availability of pre- and post-failure observations (Selli and Trevisan 1964; Rossi and Semenza 1965;

Müller 1964; Belloni and Stefani 1987). The rockslide formed by two major masses (eastern and western), underlined on the upper slope by a long M-shaped tension crack, moved along a chair-like sliding surface with a relatively flat toe and a steep back (25°–43°) and the eastern and western sectors of the sliding surface slightly dipping towards each other.

The sliding mass (ca  $275 \times 10^6 \text{ m}^3$  covering about  $2 \text{ km}^2$ ) moved laterally some 360–450 m, and 140 m upwards on the opposite valley flank, at an estimated average velocity of  $20\text{--}30 \text{ m s}^{-1}$  (Hendron and Patton 1985). The rockslide rapidly displaced the impounded water ( $169 \times 10^6 \text{ m}^3$ ), partially along the opposite valley flank, the upstream valley reach and over the 276-m Vajont doubly arched dam. The wave eroded trees and soil on the northern side of the Vajont valley up to a maximum elevation of 935 or 235 m above the reservoir level (700 m a.s.l.). The wave swept across the dam reaching over 100 m above its crest (435 m) above the downstream base of the dam and down the Vajont Gorge to the Piave River, where it had a height of some 70 m at the confluence with the Piave Valley. Villages of Longarone, Pirago, Villanova, Rivalta, Faè and Codissago in the valley were destroyed. Some 2000 persons died and many others were injured, almost all from the effects of the wave. The failure lasted about 50 s (Ciabatti 1964) and produced seismic shocks with a total duration of up to 97 s, inclusive of the signal generated by the water wave (Caloi 1966).

The rockslide moved along a relatively well-defined failure surface strongly controlled by bedding and structural features (Fig. 1a, b) and characterized by weak centimetre- to decimetre-thick smectitic clay levels (Hendron and Patton 1985), interlayered with thin micritic limestone of the Fonzaso Formation. Clay level strength was investigated under different degrees of saturations, total displacement and low to high slip rates (Skempton 1966;  $16.67 \mu\text{m s}^{-1}$ , Hendron and Patton 1985;  $0.24 \mu\text{m s}^{-1}$  to up to  $0.08 \text{ m s}^{-1}$ , Tika and Hutchinson 1999;  $0.2 \mu\text{m s}^{-1}$  to  $1.31 \text{ m s}^{-1}$ , Ferri et al. 2011). As a consequence, the determined friction coefficient varies within a relatively broad range from 4.4° to 22.3° (Tika and Hutchinson 1999), 5° to 16° (Hendron and Patton 1985), and finally from 1.7° to 37.2° and 0° to 36.7° (Ferri et al. 2011) for peak and steady-state conditions, respectively. Unfortunately, for most of the tests no pore pressure and temperature measurements are available, both within the sample and along the shearing surface, making a reliable characterization of the materials difficult. Geomechanical description and characterization of the rockslide mass have been carried out by various authors (e.g. Broili 1967; Ghirotti 2012; Superchi 2012). Superchi produced a geomechanical zonation of the rockslide mass and



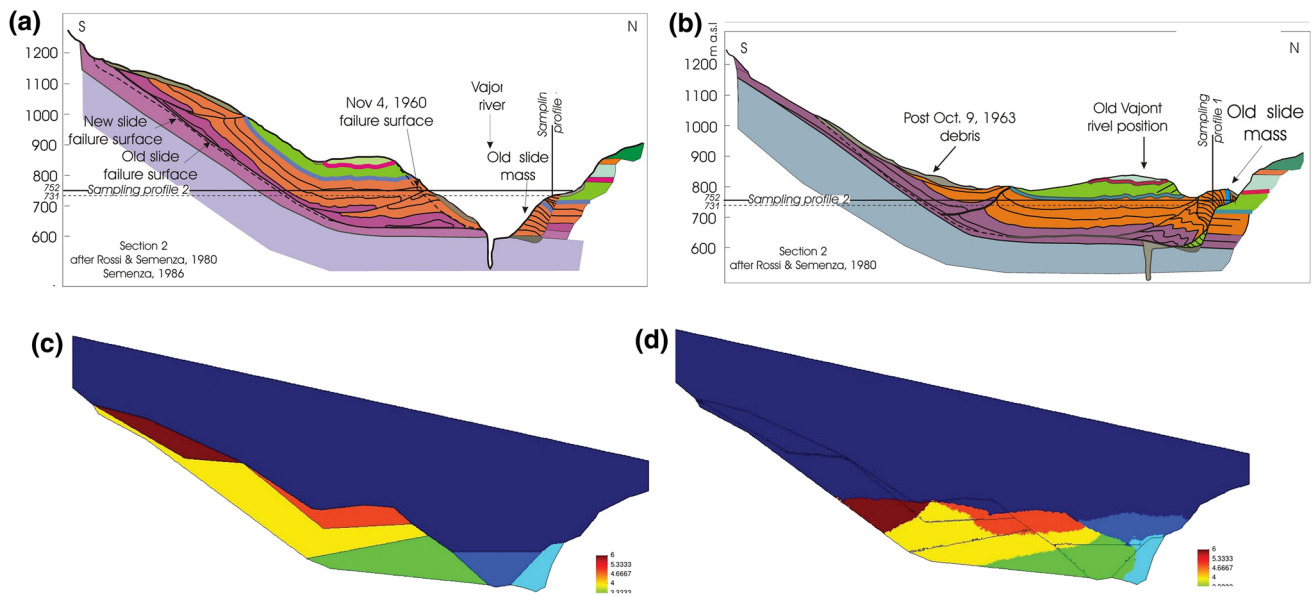


**Fig. 1** Pre- and post-failure geologic cross sections corresponding to Section #2 by Rossi and Semenza (1965). Two sampling profiles (a) used to sample water velocities in the numerical model (see Fig. 4) are shown in the upper pre-failure cross section. c, d Initial and final geometries

conterminous areas. This work shows GSI values in the 21–40 range and 41–60 range within and outside the rockslide mass, respectively. This suggests a relatively weak rock mass also before the rockslide occurrence, especially considering the fact that the slope material was affected already by an important displacement in prehistorical times.

The Vajont rockslide was the first landslide for which water tank and scaled physical models were performed both before (Ghetti 1962) and after the event by the expert witnesses (Roubault 1967; Calvino et al. 1967; Votruba 1966; Datei 2003), for prediction of the possible effects and verification of the possibility to correctly predict the observed effects, respectively. Ghetti (1962) was commissioned by the owner of the hydroelectric plant to carry out two different series of tests on a 1:200 scale model of the entire reservoir, simulating the rockslide: a flat surface inclined at 30° up to 42°; a more realistic sliding surface convergent in plane and with a characteristic chair-like profile. The gravelly landslide material (8–10 mm in diameter) was released under gravity or by pulling the mass towards the lake so to control the rockslide duration (60–225 s) and velocity. Ghetti varied also the reservoir level (700 and 722.5 m a.s.l.) and the volume of released material as well as the sequence of release. The models never simulated the simultaneous failure of the two main rockslide sectors (eastern and western), and the maximum water wave run-up was estimated as 27.5 m with the maximum reservoir level.

Roubault's 3D model (Calvino et al. 1967) adopted a simplified geometry (1:830 in scale), a sliding carriage (i.e. simulating a rigid block) or a predefined volume of

granular material with different grain size (i.e. 1, 5, 10, 20–30, 100 mm) to simulate different rockslide permeability and released at different velocities. The sliding carriage always caused higher run-ups with respect to the release of granular masses. For the latter, the run-up increased with the grain size. Votruba's 2D model (1966) adopted a simplified geometry (1:500 in scale) and different materials (i.e. glass beads, piled plastic sheets) recognizing the influence of the rockslide velocity and a minor effect of the material on the rockslide maximum displacement and recorded run-up. Another 2D physical model (1:500 in scale) was used by Datei (2003) simulating the sliding of different granular materials (i.e. rounded gravel, 3–4, 6–8 mm, angular gravel and pebbles with sand, ceramic tiles) at different velocities. The results confirmed the rapid decrease in the run-up with the slide velocity. All the experts estimated for a rockslide duration of about 20–25 s (i.a. ca. 12.5–22 m/s) a run-up similar to the observed one (ca 190 m). This duration reasonably agrees with the interpretation of the recorded seismogram according to Caloi (1966), with completion of the rockslide impact against the opposite valley flank after about 35 s.

Numerical models, once calibrated and validated allow repeating simulations and testing different behaviours and boundary conditions more efficiently than physical models. A series of numerical models have been developed and used to simulate the Vajont rockslide runout (Sitar et al. 2005; Alonso and Pinyol 2010; Crosta et al. 2003, 2007, 2012) and impulse wave, recently (Ward and Day 2011; Bosa and Petti 2011, 2013; Vacondio et al. 2013, Zaniboni and Tinti 2014). Nevertheless, in these models, simplified geometric conditions (1D), rigid mass rotation or simplified

rheological models for the rockslide material are generally assumed.

In the following, we present simulations of 2D water tank experiments (Fritz 2002; Fritz et al. 2003a, b; Sælevik et al. 2009) for validation of the adopted FEM ALE numerical solution and of the Vajont rockslide evolution (in 2D and 3D) and interaction with the reservoir.

## 2 Materials and Methods

### 2.1 Numerical Model

Sliding and flowing of rock and soil masses and dense granular flows are characterized by very large displacements and deformations. A traditional Lagrangian finite element method would cause in such conditions an extreme distortion of the finite element (FE) mesh and consequently inaccurate results. To the aim of modelling the landslide and impulse wave evolution, we use an FEM code (Roddeman 2013) adopting an arbitrary Eulerian–Lagrangian (ALE) method which guarantees accurate calculation results also for large deformations. We refer to Roddeman (2013) for more details about the code and its implemented capabilities to simulate 2D and 3D landslides and granular flows (Crosta et al. 2006, 2007, 2008a, b, 2009, 2013a). The adopted model uses a particular type of combined Eulerian–Lagrangian method (Roddeman 2013; Crosta et al. 2003, 2008a, b) which does not distort the FE mesh and guarantees accurate calculation results. In this model, the flow of the material is governed by:

$$\rho \dot{v}_i = \frac{\partial \sigma_{ij}}{\partial x_j} + g_i,$$

where  $\rho$  is the density of the material,  $v_i$  is the velocity in  $i$ -direction ( $i$  is 1, 2 or 3),  $\sigma_{ij}$  denotes the stress tensor,  $x_j$  is the  $j$ -th space coordinate (i.e.  $j$  equals to 1, 2, or 3) and  $g_i$  represents the gravity force in  $i$ -direction (where  $g_1 = g_2 = 0$ ,  $g_3 = -9.81$ ). When the material stresses are examined  $\sigma_{\text{effective},ij}$ , the effective stress changes due to material stiffness result in a fixed frame from two different contributions (Hunter 1983). In a fixed frame, the first contribution of the changes in effective stress results from rigid body rotations of the material. These rotations induce changes of the effective stress tensor components relative to a fixed frame. Nevertheless, these rigid body rotations, from an arbitrary deformation field, are not uniquely defined and a choice has to be made about how to model this contribution consequently. The proposed approach adopts an incrementally objective Lagrangian model, based on a polar decomposition of the incremental deformation tensor (Roddeman 2013). Therefore, it is possible to write the deformation tensor  $\Delta F$ , with deformation referring to the

previous time step, as:  $\Delta F = \Delta R \cdot \Delta U$  where  $\Delta R$  is the rotation tensor and  $\Delta U$  the stretch tensor. At this point, using the rotation tensor  $\Delta R$ , the rigid body stress change can be written as:

$$\Delta \sigma_{\text{effective}} = \Delta R \sigma_{\text{effective}} \Delta R^T.$$

The second contribution, from straining of the material, is computed by using the incremental stretch tensor  $\Delta U$  to determine the incremental strain tensor  $\Delta E$ :

$$\Delta E = 0.5(\Delta U + \Delta U^T) - I,$$

where  $I$  is the identity tensor. Calculation of the stresses from straining of the material is completed by adopting an elasto-plastic model. In this case, an elastic isotropic stiffness tensor  $C$  (Chen and Han 1988) is adopted for the elastic part:

$$\Delta \sigma_{\text{effective}} = C(\Delta E - \Delta E_{\text{plastic}}),$$

where the fourth-order tensor,  $C$ , solely depends on Young's modulus and Poisson's ratio for an isotropic material. For the plastic part, a Mohr–Coulomb model is applied so that the plastic strains,  $\Delta E_{\text{plastic}}$ , are determined in such a way that the yield function,  $f$ :

$$f = 0.5(\sigma_{\text{effective},1} - \sigma_{\text{effective},3}) + 0.5(\sigma_{\text{effective},1} + \sigma_{\text{effective},3}) \sin \phi - c \cos \phi \leq 0$$

cannot take positive values in elastoplasticity. Here,  $c$  is the cohesion,  $\phi$  is the material friction angle, and  $\sigma_{\text{effective},1}$  and  $\sigma_{\text{effective},3}$  are the maximum and the minimum principal stresses, respectively. A zero dilatancy condition is assumed, considering a flow rule with a dilatancy angle equal to zero. The rotation and stretching increments of the stresses, obtained through the above-described steps, are added to the stresses of the previous time point to give the new effective stresses,  $\sigma_{ij}$ , at the current time. The model can include the effect of pore water (Crosta et al. 2008a, b), but no water is considered within the landslide mass in the cases discussed in this paper. Anyway, this set of equations allows describing the large deformations and sliding of landslide material, filled or not filled with groundwater. In these models, also the nonlinear elastic soil behaviour, cracking phenomena and partial groundwater saturation are neglected, but could be modelled, for example, with hypoplasticity laws, damage laws and smeared cracking concepts, and partially saturated soil models, respectively. For the case of sliding along a rigid (non erodible) surface, the velocity of the material is set equal to zero, and a reduction in the cohesion and friction angle of the plastic law is applied to model reduced friction between the material and the sliding surface.

The numerical model uses isoparametric finite elements for space discretisation, and in particular three-noded triangles and eight-noded hexahedrals in the presented 2D

and 3D simulations, respectively. An implicit Euler time stepping, with automatic time step adjustment is adopted to keep control on out-of-balance forces at the nodes. Since material displacements are disconnected from the finite element mesh, state variables are transported through the mesh by a streamline upwind Petrov–Galerkin method. The velocities at each time step are calculated such that inertia and internal stress contributions create equilibrium at the finite element nodes.

The initial equilibrium stress state is reached through quasi-static time stepping, applying gravity incrementally in successive time steps, in such a way that no inertial effect is introduced. The initial movement or occurrence of the landslide can be triggered by either lowering cohesion in time (Crosta et al. 2003, 2008a, b), or imposing a base acceleration diagram to simulate seismic triggering, or by deleting instantaneously a confining wall. Therefore, computation does not require a predefined failure surface and it continues until complete stopping of the mass.

In the literature, the reservoir water has been generally modelled using the Navier–Stokes equations, considering water to be either fully incompressible or nearly incompressible (Quecedo et al. 2004, Abadie et al. 2010). The viscous contribution in these equations is relevant for small Reynolds numbers, whereas for large Reynolds numbers inertia and pressure dominate over viscosity. For the type of applications discussed in this paper, the velocity of soil and rockslides/avalanches impacting on the water surface tends to be high, so that viscosity is neglected (i.e. fully inviscid fluid). For the compressible part, we apply a nearly incompressible penalty formulation:

$$\dot{p} = \lambda v_{i,i}, \quad (1)$$

where  $\dot{p}$  is the water pressure rate and  $v_{i,i}$  denotes water velocity  $v_i$  gradient along the spatial  $x_i$  direction. A large value ( $1.6 \times 10^9$  Pa) is chosen for the penalty factor,  $\lambda$ , so that the water behaves as a nearly incompressible fluid. On the other hand, the values should not be excessively high to prevent numerical problems with ill-conditioned system matrices or very small time steps needed to capture extremely fast pressure changes. Different values of the penalty factor have been tested demonstrating that changing this value does not have a strong influence on the final results, allowing to optimize the computational effort. The equations adopted for the water domain are:

$$\rho \dot{v}_i = \sigma_{ij,j} + g_i, \quad (2)$$

where  $\rho$  is the water density,  $v_i$  the water velocity along the spatial  $x_i$  direction,  $\sigma_{ij}$  is the water stress matrix which contains only a diagonal part  $\sigma_{11} = \sigma_{22} = \sigma_{33} = p$ , and finally  $g_i$  is the gravity force. Between the landslide material and water, we assume a no-slip type of condition,

with equal water and landslide velocity at the contact. No friction exists at the contact.

### 3 Water Tank Tests

Testing and validation of the modelling approach is required before use in more complex modelling problems. For this reason, a series of numerical simulations has been performed to verify capabilities against well-constrained and documented physical models at laboratory scale (Fritz 2002; Fritz et al. 2003b, Sælevik et al. 2009).

#### 3.1 2D Fritz's experiments

When a slide hits a water reservoir, a hydrodynamic impact crater may form if flow separation occurs along the back and the tail of the slide (Fritz 2002; Fritz et al. 2003b). The hydrodynamic impact crater is controlled by the slide geometry, contrast in stiffness between the slide material and water, transfer of kinetic energy and the slide Froude number (i.e. ratio between the slide velocity and the square root of the gravitational acceleration times the water depth). If the slide is slow, then it is difficult to observe flow separation and the generated wave is a function of the slide geometry and its changes when submerged. On the contrary, flow separation becomes evident at high velocity and Froude numbers, generating backward or outward collapsing craters, with displaced water volumes much larger than the landslide mass. According to Slingerland and Voight (1979), most of the landslide events are characterized by a Froude number in the range 0.5–4.

Among the tests performed, releasing granular landslides in a 7.5 m (Fritz 2002) and 11 m (Fritz et al. 2003a, b)-long water tanks, we chose the case of an outward collapsing impact crater. In the experimental setup, the slope inclination is  $45^\circ$ , the water depth 0.3 m, the granular slide 0.6-m long and 0.118-m thick with an initial velocity of  $5.2 \text{ m s}^{-1}$  and a Froude number of 3.2.

Following Fritz et al. (2002, 2003a), the adopted properties for the granular landslide are  $\rho = 18 \text{ kN/m}^3$ ,  $\nu = 0.23$ ,  $E = 10^4 \text{ kPa}$  and  $\phi = 43^\circ$ , whereas along the basal surface  $\phi_{\text{bas}} = 24^\circ$  and the water bulk compressibility modulus is equal to  $10^4 \text{ kPa}$ . We use 76,200 linear-triangular elements, with an average length of 0.02 m, with 370 elements to discretize the landslide and 12,800 for the water. The soil material impact on the water surface occurs after 0.13 s, with an impact velocity of  $5.4 \text{ m/s}$  (experimental:  $5.49 \text{ m s}^{-1}$ ), a length of the mass of material equal to 0.68 m (exp.: 0.764 m), a thickness of 0.118 m (exp.: 0.093) and the calculated slide Froude number of 3.15 (exp.: 3.2). Figure 2 shows the impact of the granular material, the deformation of the front transforming in

curved and steep snout, the flow separation and the successive rising of the wave. The front is steep and convex, whereas the back gets progressively thin till the end of motion when the landslide tail stops just beyond/at the submerged slope toe. In the same figure, the development and progressive displacement of the solitary wave and secondary oscillatory waves in the near field are recognizable.

At 0.24 s, the frontal part of the slide is torn off by the water action and starts to develop a sort of backward tilted plume that rejoins the upper slide material before 0.7 s. This type of feature has been observed experimentally by Fritz (2002, Fritz et al. 2003a, b) and by Viroulet et al. (2013; see also <https://www.irphe.fr/~viroulet/research.html>). The water is expelled both out- and upwards by the slide which remains completely dry on its back, exposing also the previously submerged ramp. The collapse of the crater on the upper part of the landslide occurs when the landslide has already reached the bottom of the tank. The water starts flowing back initially from the bottom of the crater wall (around 0.56 s in Fig. 2); then the backwash wave develops covering the slide mass and surging up along the ramp. At the same time, a large part of the flow moves outwards generating a primary wave. This solitary wave moving along the tank is shown passing through a vertical cross section located at 3.3 m from the slope toe (Fig. 3a). The symmetry of the primary (i.e. leading) wave appears clearly from the similarity of the velocity profiles

during the transit of the ascending and descending flanks. Furthermore, we observe that the velocity is almost constant along the entire profile excepted when it reaches the peak. The translation of the leading wave with its characters is shown in Fig. 3b where the wave amplitude sampled at two distances along the tank (1.8 and 3.3 m) is plotted with respect to normalized time.

The performance of the model at catching the maximum crest amplitude, one of the most important parameters for hazard assessment, is pointed out in Fig. 4. This demonstrates the very good alignment of the numerical results, in terms of normalized maximum crest amplitude, with the experimental values presented by Fritz et al. (2004) and those calculated with their proposed empirical relationship.

The agreement between the experimental test and the numerical results is shown in Fig. 5 where snapshots and PIV results from Fritz et al. (2003b) are compared directly to computed velocity vectors even if not exactly at the same instants. The rapid arrest of the landslide mass and the progressively changing direction of the vectors from upwards and outwards to downwards and backwards is caught by the model. After 0.24 s, the impact generates a crater with a vertical inner flank and most of the velocity vectors directed upwards. At 0.44 s, the vectors are still directed towards the open basin but with a more horizontal, less steep, direction. The sliding mass reaches the basin bottom, still maintaining a steep front. At 0.56 s, the inner crater wall starts collapsing vertically, beginning from the

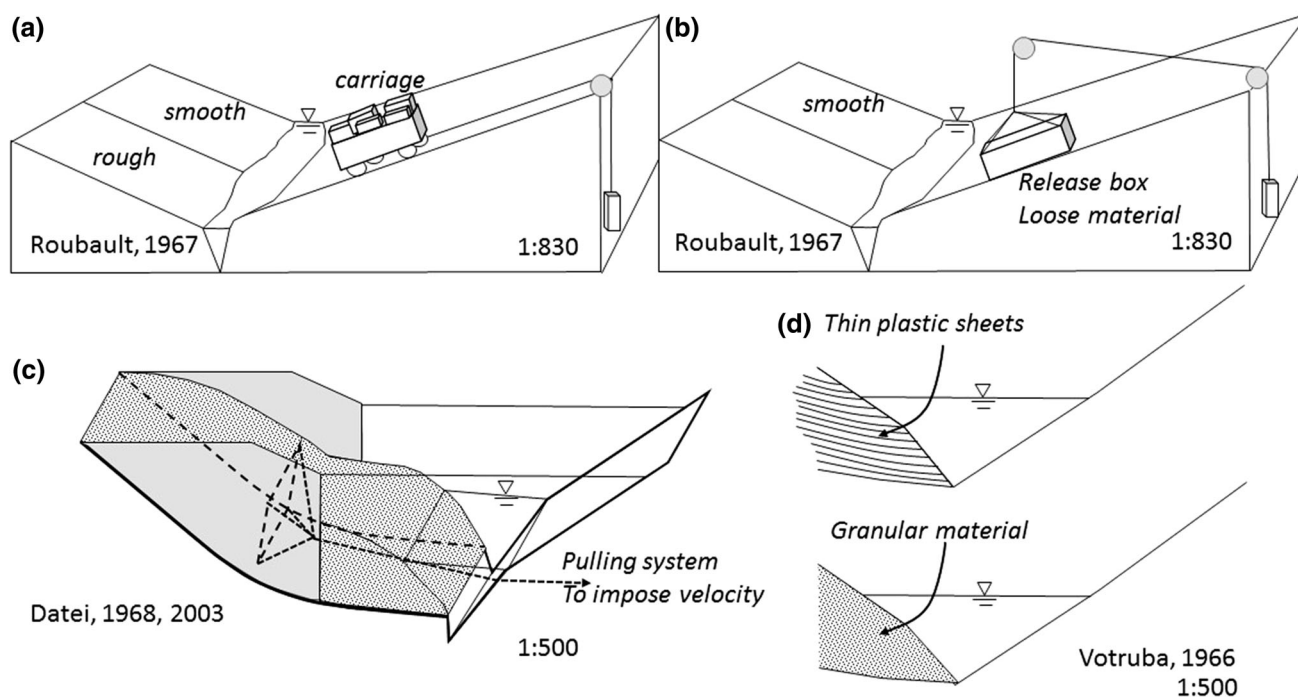


**Fig. 2** Sketch showing the settings for the laboratory physical models as prepared by (a) and (b) Roubault (1967) with two different release mechanisms for a carriage and coarse granular material; c Datei

(1968, 2003) using granular material; d Votruba (1966) with granular materials and plastic sheets to simulate the rockslide



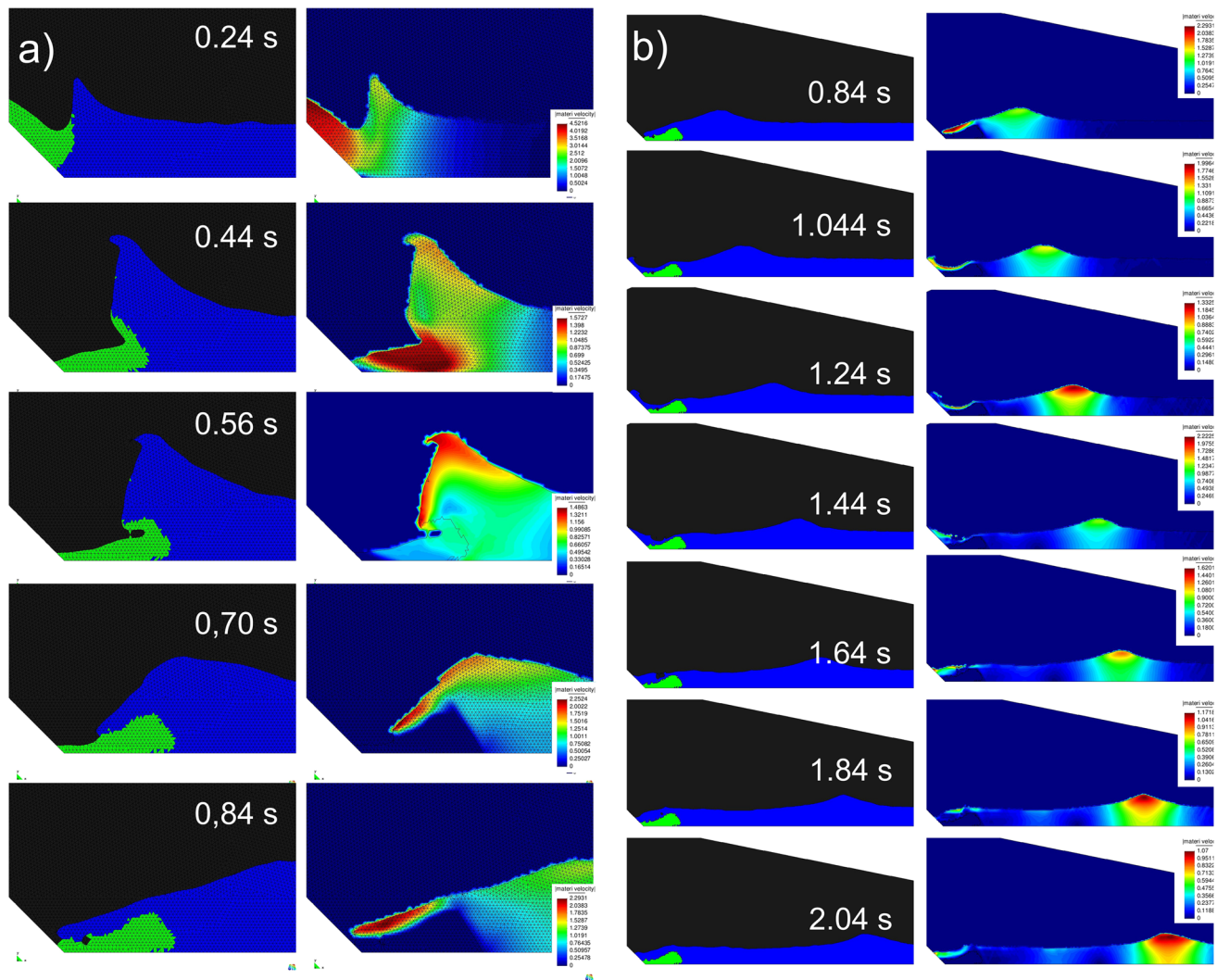


**Fig. 3** Velocity field ( $\text{m s}^{-1}$ ) computed for an impact velocity of  $5.4 \text{ m s}^{-1}$  of a 0.118-thick granular slide,  $\text{Fr} = 3.15$  showing an outward collapsing impact crater

wall inner toe, at the contact with the slide back. After 0.7 s, the slide comes to rest and the back wash wave develops covering the slide mass.

The final deposit is flatter in the experiments and this suggests the effects of the wave action and of the progressive air expulsion and water saturation on the slide mass.

### 3.2 2D Aknes Rockslide Model

As mentioned above, the Aknes rockslide is considered one of the most critical sites in Norway for the possible generation of a tsunami wave (Blikra et al. 2005; Harbitz et al. 2014) in case of a rapid collapse. Sælevik's et al. (2009) performed a series of experiments to model the landslide tsunami in a water tank with water depth of 0.6 m and a smooth transition connecting the  $35^\circ$  sliding ramp with the tank bottom. The sliding mass was represented by means of

a series of rigid box modules, connected in a train-like mode (0.5 and 0.6 m in length, 0.12 and 0.16 m in height and 45 cm in width), amounting to total lengths of 1, 1.6 and 2 m, with a front block profiled at a  $45^\circ$  angle. The initial velocity of the sliding blocks was controlled by means of a conveyor belt.

Among the series of experiments, scenario #2 by Sælevik et al., characterized by a sliding mass 0.16-m high and 1-m long, an initial velocity of  $3.38 \text{ m s}^{-1}$  and a Froude number equal to 1.4, has been chosen for validation. This experiment is an example of a backwards collapsing crater generated by a perfectly impermeable sliding mass. A total of 63,500 triangular elements, with an average size of 0.02 m, were used to discretize the experimental geometry, of which 840 elements were for the boxes and 32,500 for the water within the 9.14-m-long tank. Due to the experimental geometry which caused the front wedge-shaped block to impact the tank bottom, a

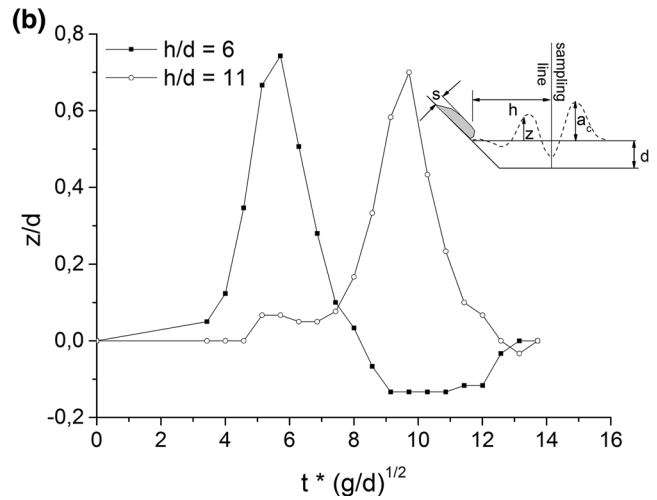
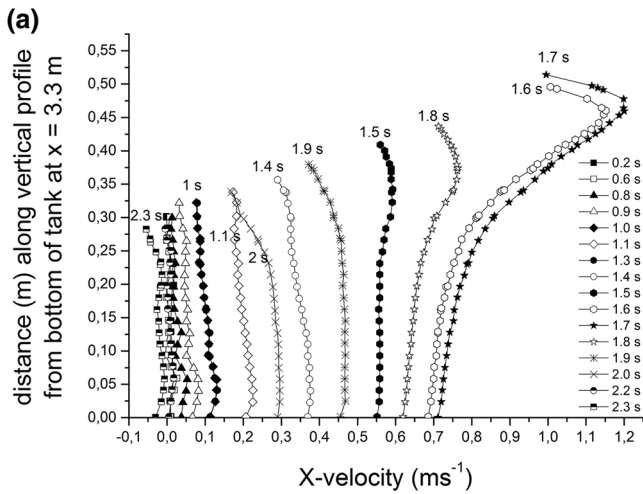


**Fig. 4 a** X-velocity component at different time steps computed along a vertical profile positioned at 3.3 m from the slope toe. The constant velocity value along the profile at different time steps is made evident. **b** Variation of normalized wave height, measured at

two different distances from the shoreline ( $h = 1.8 \text{ m}$  and  $h = 3.3 \text{ m}$ ,  $h/d = 6$  and  $11$ , respectively), with respect to normalized time. See *inset* in **b** for explanation of variables

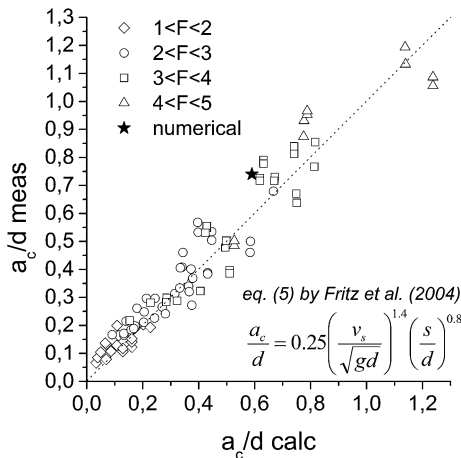


**Fig. 5** Normalized maximum crest amplitude measured in water tank tests with respect to values calculated according to Fritz et al. (2004). The *star* represents the computed value by the FEM 2D ALE model. Variables as in Fig. 4b

slightly deformable sliding mass was assumed in the numerical simulations ( $\rho = 18 \text{ kN/m}^3$ ;  $\nu = 0.23$ ,  $E = 10^5 \text{ kPa}$ ,  $\phi = 43^\circ$ ,  $c = 0 \text{ kPa}$ ). Furthermore, a bulk water compressibility modulus of  $10^4 \text{ kPa}$  and a basal friction angle  $\phi = 24^\circ$  along the sliding ramp (Sælevik et al. 2009) were assumed.

Figures 6 and 7 show the backward collapse of the hydrodynamic crater generated by the larger than slide displaced water volume. The water is pushed outwards but much less than for the outward collapse, then the crater closes progressively over the surface partially by collapsing and by backward flow over the back of the slide material. During the collapse phase in the experiments, some

air pocket can become trapped. Finally, the surface closure originates a splash rising along the sloping ground of the exposed ramp. At this moment, the flow diverges and this happens at 0.50 s when a clear rounded crest develops with a small part of the water flowing backwards and the primary wave moving to the right.

More in detail, some peculiar features can be described with time (compare also with Fig. 6), namely:

- 0.1–0.2 s: the frontal impact causes the instantaneous upward expulsion of water and the formation of an oblique velocity discontinuity originating at the corner between the slope toe and the flat basin bottom.
- 0.3 s: the vectors within the crater inner side start to sag, with the more internal ones already directed downwards and the most external still directed upwards.
- 0.4–0.5 s: a clear vortex-like structure develops just behind the slide crest, with an anticlockwise pattern and a saddle point with no flow which can be also recognized in Fig. 6 (see at  $t = 0.5 \text{ s}$ ). The frontal push exerted by the slide on the water mass generates velocities directed progressively upwards at higher angles while moving backwards along the slide.
- 0.5–0.7 s: a high relative velocity exists at the front of the sliding mass; at 0.5 s the inner crater side collapses almost vertically and at 0.6 s the vortex-like pattern tends to disappear and a saddle develops at the surface. The final slide geometry is very different from the one obtained for the deformable slide case (see Figs. 2, 5), with only the frontal part laying on the basin bottom beyond the slope toe.
- 0.8–1.0 s: the saddle point at the surface moves progressively offshore while the backwash wave cover

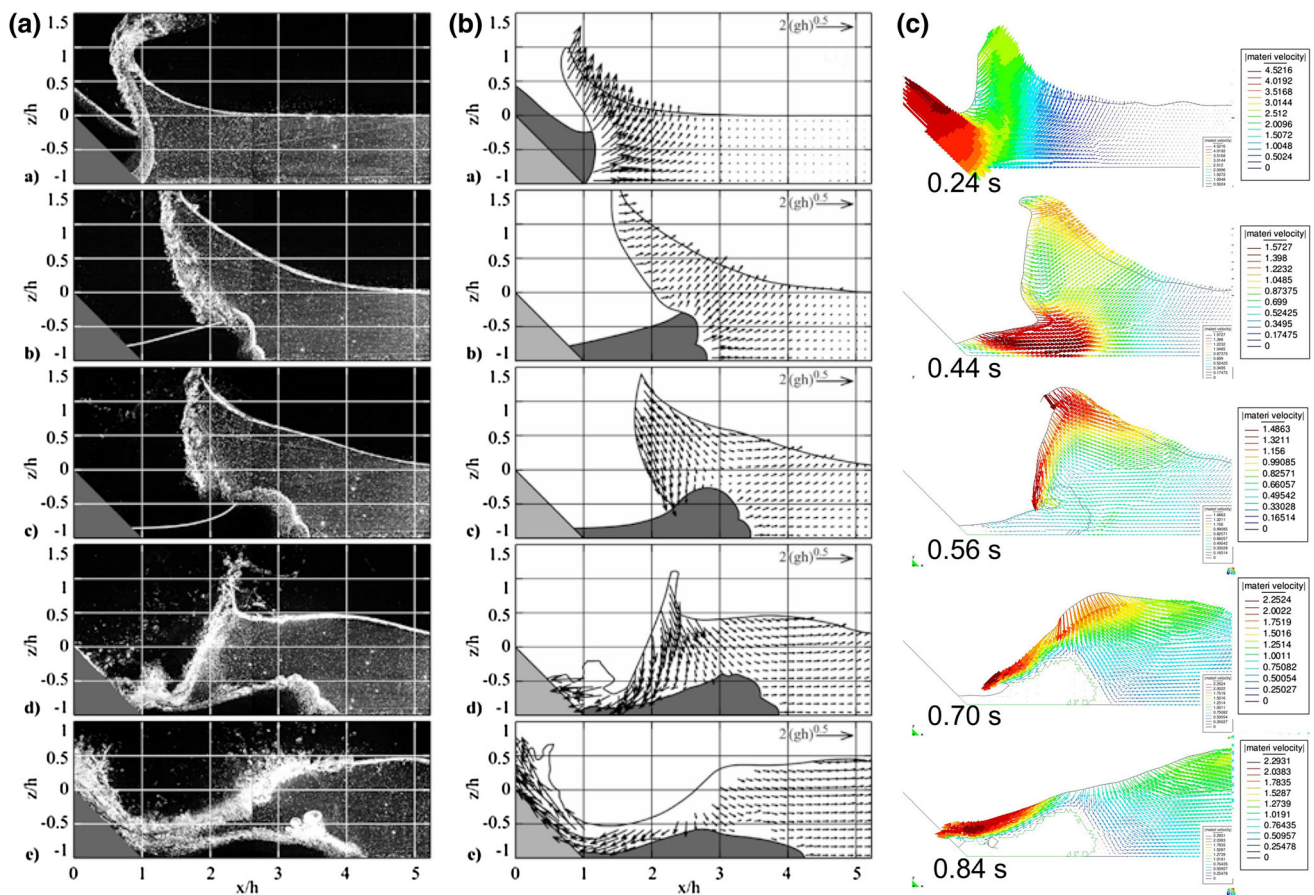


**Fig. 6** Comparison of the observed (Fritz 2002; Fritz et al. 2003b; left hand and middle panels) and computed wave velocity vectors (on the right hand side) for the same times. Slight differences could be

derived by small initial differences in impact velocity, material deformability and exact timing

the tail of the slide and successively comes back towards the open basin.

- 0.9–2.0 s: the primary leading wave fully develops and propagates towards the open basin with a symmetrical distribution of velocity magnitude.

The propagation of the primary leading wave is well represented by the horizontal velocity profiles sampled along a vertical profile located 3 m from the slope toe (see Fig. 8). As in the previous case, the velocity remains almost constant along the entire profile suggesting an intermediate-shallow water character (Heller 2007). Finally, Fig. 9 compares the normalized wave amplitude with respect to the normalized time, showing the good agreement between the computed and measured values. Three different numerical curves are presented and for comparison the experimental result published by Sælevik et al. (2009) ( $h = 3.3$  m) is plotted.

### 3.3 Vajont Rockslide

The numerical code, validated against some reliable and detailed experimental evidence, has been applied to the

simulation of the Vajont rockslide. In the following, the results of 2D and fully 3D simulations are presented and compared to real observations. Some 3D runout modelling not considering the reservoir water was previously presented by Crosta et al. (2007) together with some 2D slope stability analyses.

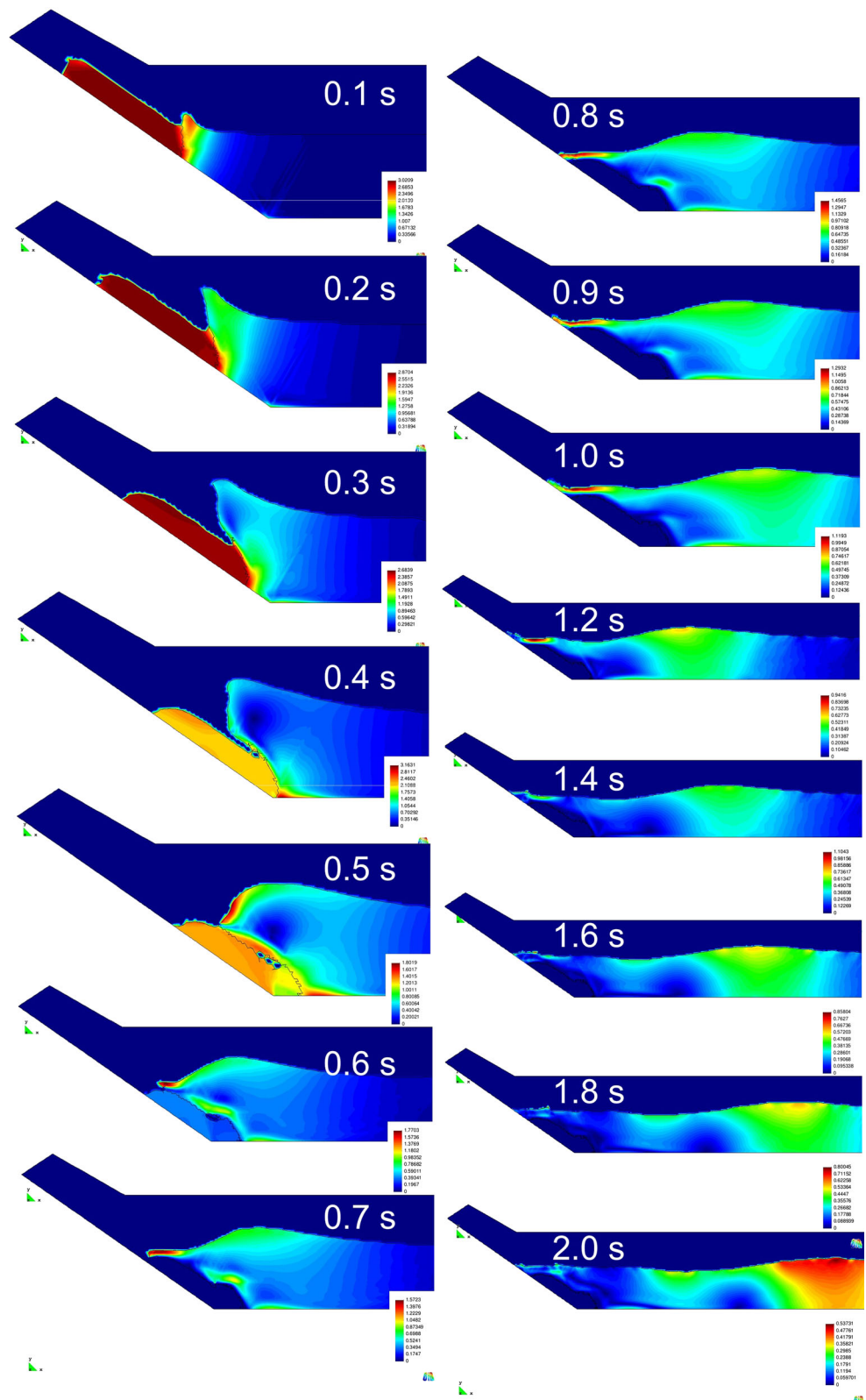
### 3.4 2D Modelling

Modelling has been performed on different cross sections and in particular various simulations have been performed along cross section #2 (see Fig. 1) presented by Rossi and Semenza (1986). The impounded water, filling to about two-thirds (ca 115 Mm<sup>3</sup>, mean depth: 100 m) the reservoir, was completely displaced by the rockslide reaching 935 m a.s.l (235 m above the reservoir level, 702.5 m a.s.l.) and the wave swept across the dam reaching over 100 m above its crest.

On the basis of this data and some of the estimates of the slide velocity, it is possible to compute a rough value of the slide Froude number ( $F_r = v/(gh)^{1/2}$ ;  $v$  = slide velocity,  $h$  = reservoir water depth) ranging between 0.26 and 0.75.



**Fig. 7** 2D modelling of Aknes rockslide—Sælevik's et al. (2009) experiment. The velocity field ( $\text{m s}^{-1}$ ) computed for an impact velocity of  $3.38 \text{ m s}^{-1}$  of a 1-m-long “deformable” granular slide ( $\text{Fr} = 1.4$ ) is presented. A backward collapsing impact crater develops during the modelling. Original experiments were completed using a rigid block

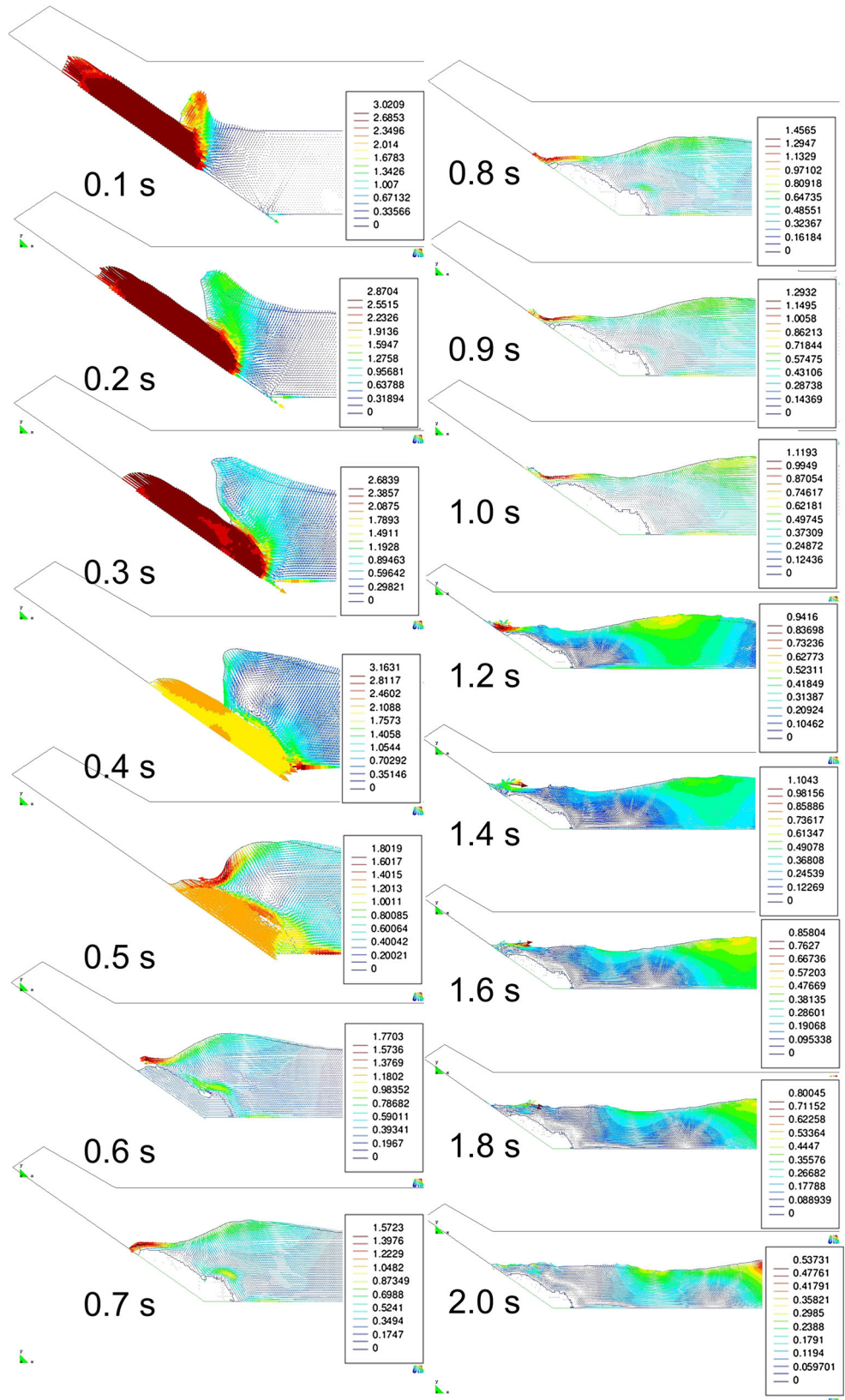


The problem geometry has been discretized through 71,800 triangular elements with an average size of 4 m, of which 15,500 were employed for the landslide, 1000 for

the old landslide material located on the opposite valley flank (when included) and about 1800 for the water reservoir. A Mohr–Coulomb elastoplastic material was



**Fig. 8** 2D modelling of Aknes rockslide—Sælevik’s et al. (2009) experiment. The velocity vectors ( $\text{m s}^{-1}$ ) computed for an impact velocity of  $3.38 \text{ m s}^{-1}$  of a 1-m-long “deformable” granular slide ( $\text{Fr} = 1.4$ ) is presented. A backward collapsing impact crater develops during the modelling. Original experiments have been completed using a rigid block



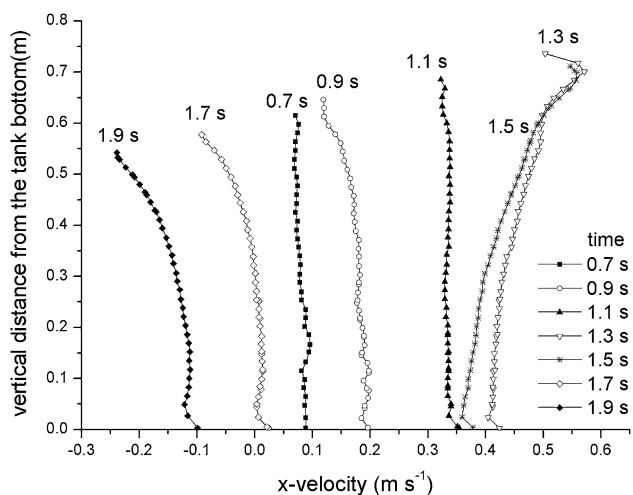


**Fig. 9** X-velocity component computed at different time steps along a vertical profile, located at  $x = 3$  m, for the 2D modelling of the Aknes rockslide—Sælevik's et al. (2009) Scenario #2 experiment

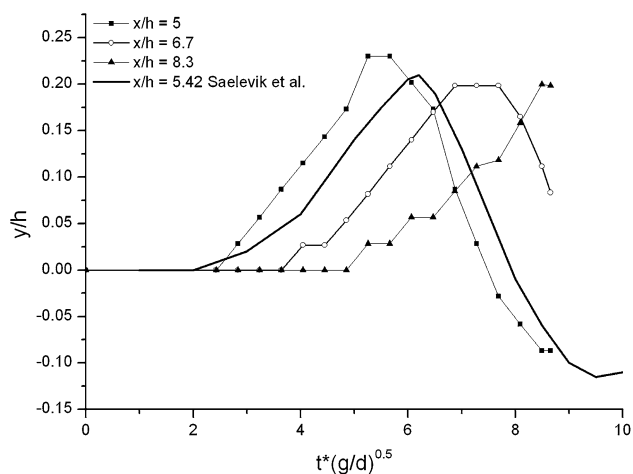


**Fig. 10** Variation of normalized wave height, measured at three different distances from the shoreline ( $h = 3, 4, 5$  m), with respect to normalized time. Results can be compared to the data provided by Sælevik's et al. (2009) for Scenario #2 experiment for a vertical sampling profile, located at  $x = 3.3$  m

used for the landslide ( $\rho = 24 \text{ kN/m}^3$ ;  $\nu = 0.23$ ,  $\phi = 17^\circ$ ,  $c = 300 \text{ kPa}$ ) and along the basal plane ( $\phi_b = 7.5^\circ$ ,  $c = 10 \text{ kPa}$ ; see Skempton 1966; Hendron and Patton 1985; Tika and Hutchinson 1999). A material with lower strength was adopted for the old landslide on the opposite valley flank ( $\phi_b = 13^\circ - 7.5^\circ$ ,  $c = 100 - 10 \text{ kPa}$  reduced according to a plastic strain softening model).

Figure 10 presents both the results for the case of a dry valley and of an impounded lake, whereas Fig. 11 shows the results of a model inclusive of the old landslide deposit lying on the right hand valley flank.

The landslide motion stops after about 28 and 32 s for the dry (Fig. 10a) and the impounded lake cases (Fig. 10b), respectively. In the latter case, water motion starts after 4–5 s from landslide onset and continues up to a total time of about 144 s when almost complete stopping is reached. In both the simulations, the rockslide material is shown to progressively infill the valley incision (i.e. Vajont gorge) and then a shear zone develops through the material. The two final geometries are similar with a more thin and tapered front for the dry case. For the simulation including the lake, the water is progressively pushed upwards against the opposite valley flank and reaches a maximum elevation of about 850 m a.s.l., approximately after 28–30 s since the initial movement. After that the water flows back and starts oscillating till complete rest. This second phase does not correspond to the real event because most of the water was expelled laterally, but it resembles the conditions simulated in some of the experimental models (Votruba 1966; Datei 2003) even if in this case the mass behaves as a perfectly impermeable material. The backwash wave is unable to erode or drag the more superficial parts of the landslide material. The material slides along the failure surface with an internal deformation which results in a final internal arrangement very similar to the representation given by Rossi and Semenza (1986; see Fig. 1a).

During the movement, the upslope sector compacts and partially steps over the lower sector. On the other hand, when inserted in the simulation (Figs. 1c, d, 11), the old landslide material is squeezed, deformed and pushed upwards along the opposite valley flank. Shear stresses within the rockslide evidence the concentration on some oblique bands controlled by the relatively sharp junction between the two sectors of the chair-like failure surface, and along a plane roughly parallel to the rockslide front (more evident in Fig. 11a, b).

To analyse the motion of the impounded water, water velocity has been sampled along a vertical and a horizontal profile (1 and 2 in Figs. 1, 12) at 2-s time steps. Along the vertical sampling profile #1 (Fig. 12a), the wave propagates upwards for about 25 s and then a progressive decrease up to 32 s is computed. The maximum elevation (ca. 850 m a.s.l.) is reached after 38 s when the rockslide completely stopped infilling the valley and the water still oscillated above the deposit.

Along the horizontal sampling profile #2 (at an elevation of 752 m a.s.l.; Fig. 12b), it is observed that the water close to the opposite valley side is still at rest till 20 s, when the wave motion induces the maximum velocity (ca  $21 \text{ m s}^{-1}$ ) in the sector opposite to the rockslide. The peak velocity decreases progressively up to 30–38 s and is followed by a progressive slowdown with velocities ranging between 2 and  $6 \text{ m s}^{-1}$ .

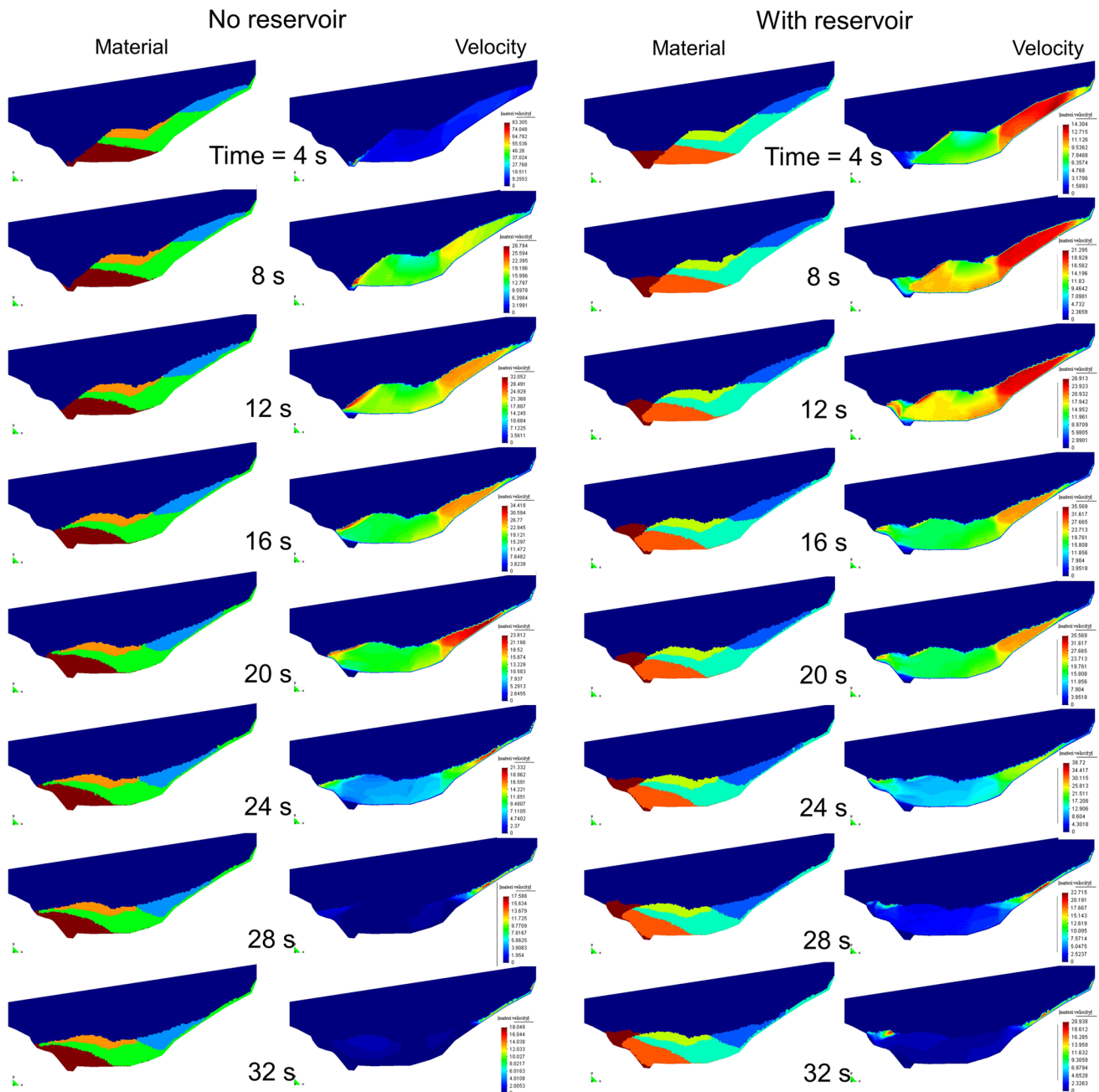


**Fig. 11** Results of the 2D FEM ALE simulations along cross section #2 (see Fig. 1a, b) by Rossi and Semenza (1965). Material geometry and velocity field for the 2D numerical models of the Vajont rockslide at different time steps and for two different conditions: *left*) without

reservoir water; *right*) with the reservoir water at an elevation of 702 m a.s.l.. Colour legends are differently scaled to evidence velocity distribution

### 3.5 3D Modelling

To provide a more realistic simulation of the phenomena involved in the collapse and rockslide–reservoir interaction, a fully 3D rockslide–water reservoir simulation has been considered. The computational domain has been discretized in about 800,000 eight-noded hexahedrals in 3D with an average base size of 22 m × 22 m and height of

18 m. Implicit Euler time stepping, with automatic time step adjustment, is adopted and the landslide is considered as a fully deformable elastoplastic continuum. The rockslide was modelled as a Mohr–Coulomb material ( $\rho = 24 \text{ kN/m}^3$ ;  $\nu = 0.23$ ,  $E = 10^{10} \text{ Pa}$ ;  $\phi = 23^\circ$ ,  $c = 100 \text{ kPa}$ ) and along the basal plane ( $\phi_b = 6^\circ$ ; see Skempton 1966; Hendron and Patton 1985; Tika and Hutchinson 1999), and as before lower properties for the

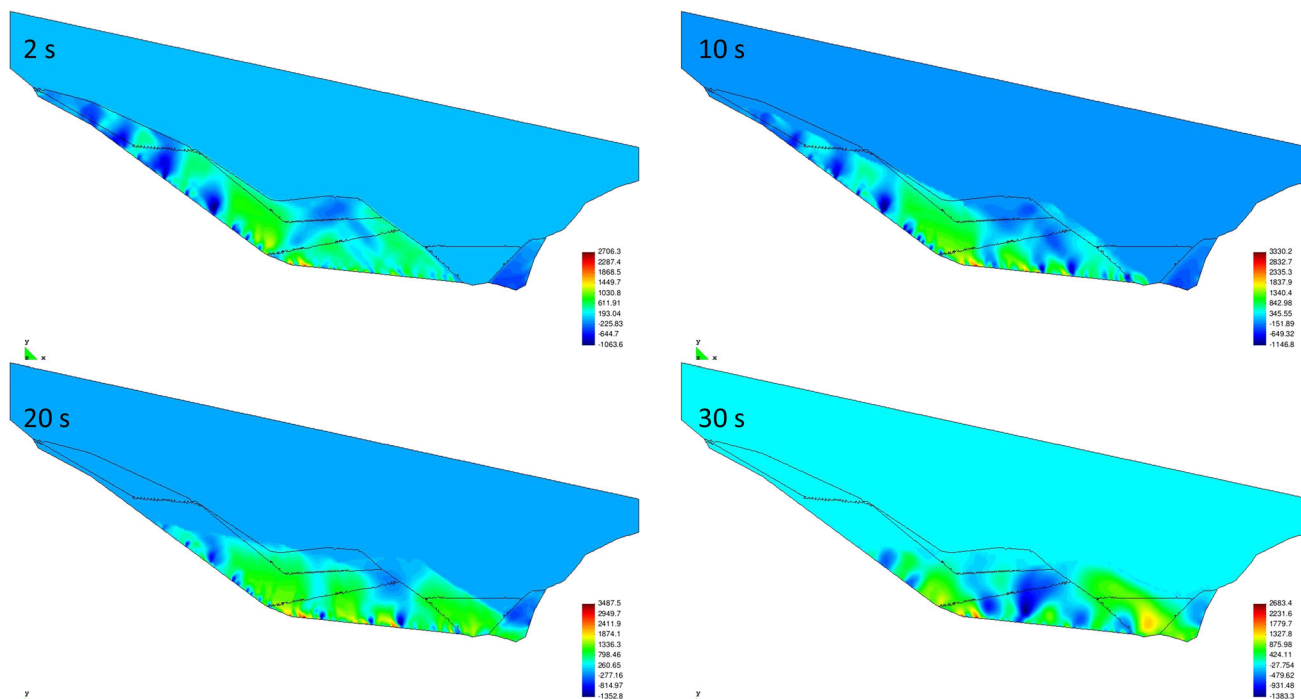


**Fig. 12**  $xy$ -Shear stresses for the 2D model along the same section as in Fig. 11 with both the reservoir water and the isolated paleo-landslide deposit lying along the northern valley flank (right hand side

in the section). Four different time steps (2, 10, 20, 30 s) are represented. Colour legends are differently scaled to evidence velocity distribution

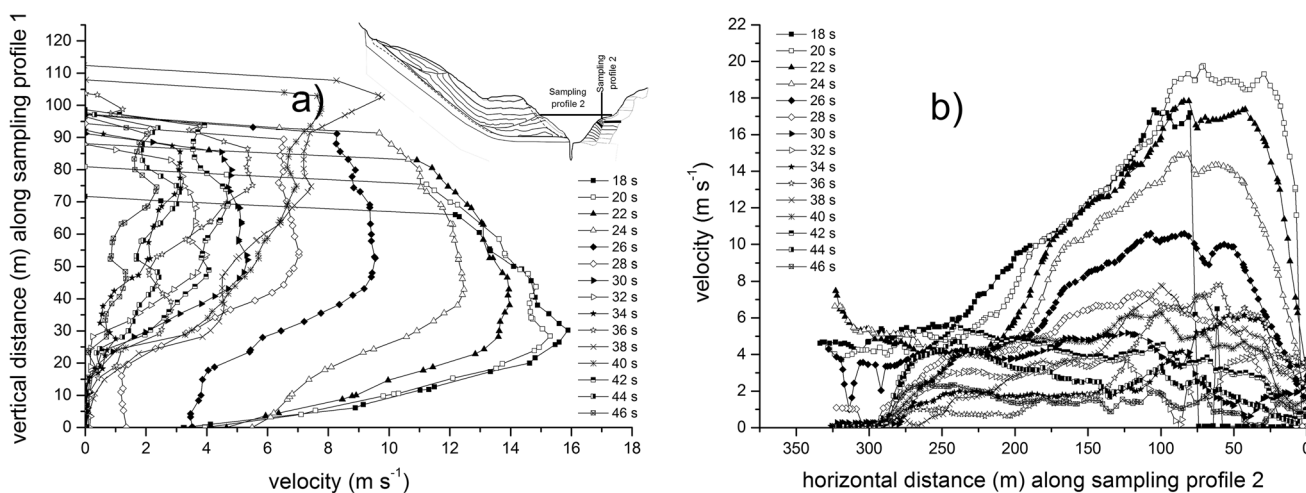


**Fig. 13** Water velocity computed at different time steps along **a** vertical profile #1 and **b** horizontal profile #2 (as shown in Fig. 1a and in the inset) for the 2D modelling of the Vajont rockslide as in Fig. 12

old landslide material resting on the opposite valley flank ( $\phi = 13^\circ\text{--}7.5^\circ$ ,  $c = 100\text{--}10$  kPa reduced according to a plastic strain softening model). Once again, because of the high velocity of soil and rockslides/avalanches impacting on the water surface, water viscosity is neglected in the analysis and a nearly incompressible penalty formulation is applied so that water behaves as a nearly incompressible fluid.

The simulation has been halted after about 50 s so as to include completely the rockslide motion and interaction, but not the downstream wave propagation, to limit the computational effort. The pre-failure and post-failure topography have been obtained by available topographic maps (Rossi and Semenza 1986), and recent Lidar surveys (by Regione Friuli Venezia Giulia) which together with borehole data (Broili 1967), geological cross sections



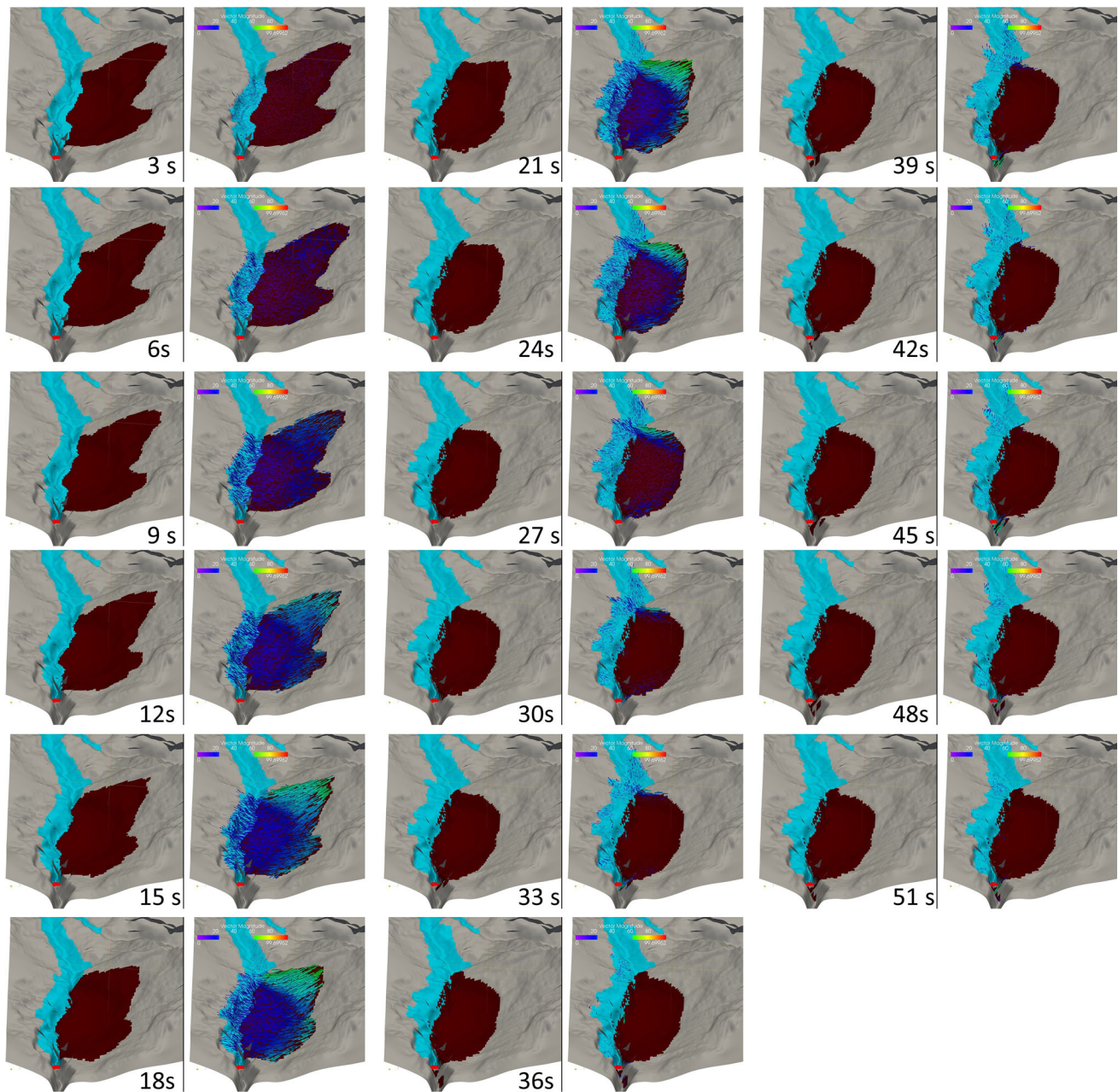


**Fig. 14** Results of the fully 3D simulation, showing the position of the landslide material (*brown*), water (*cyan*) and the velocity vectors at different time steps (3–51 s)

(Rossi and Semenza 1965) and field checks allowed to trace the 3D failure surface geometry.

Figures 13 and 14 present some of the results in terms of velocity vectors at time steps with 3-s intervals. The total duration of the rockslide since its release to full arrest is about 51 s, a value quite well comparable with previous estimations (Ciabatti 1964, Caloi 1966) and direct records. The maximum water wave run-up on the opposite valley side, the final deposit geometry, the water front splitting in an upstream and downstream direction, and the back washing along the rockslide back surface are well depicted

in the model (see bottom Fig. 14; Viparelli and Merla 1968; Selli and Trevisan 1964).

Examining the evolution of the phenomenon (Figs. 13, 14), it is observed that 3–6 s since the onset of the sliding the water starts moving. Maximum relative velocities (see also Fig. 15) are computed at the front of rockslide and in the water till 12–15 s. Following this phase the highest velocities are found in the upper part of the rockslide, where material still moves along the steep failure surface. Between 12 and 21 s, under a strong topographic control, the central part of the water wave front is characterized by

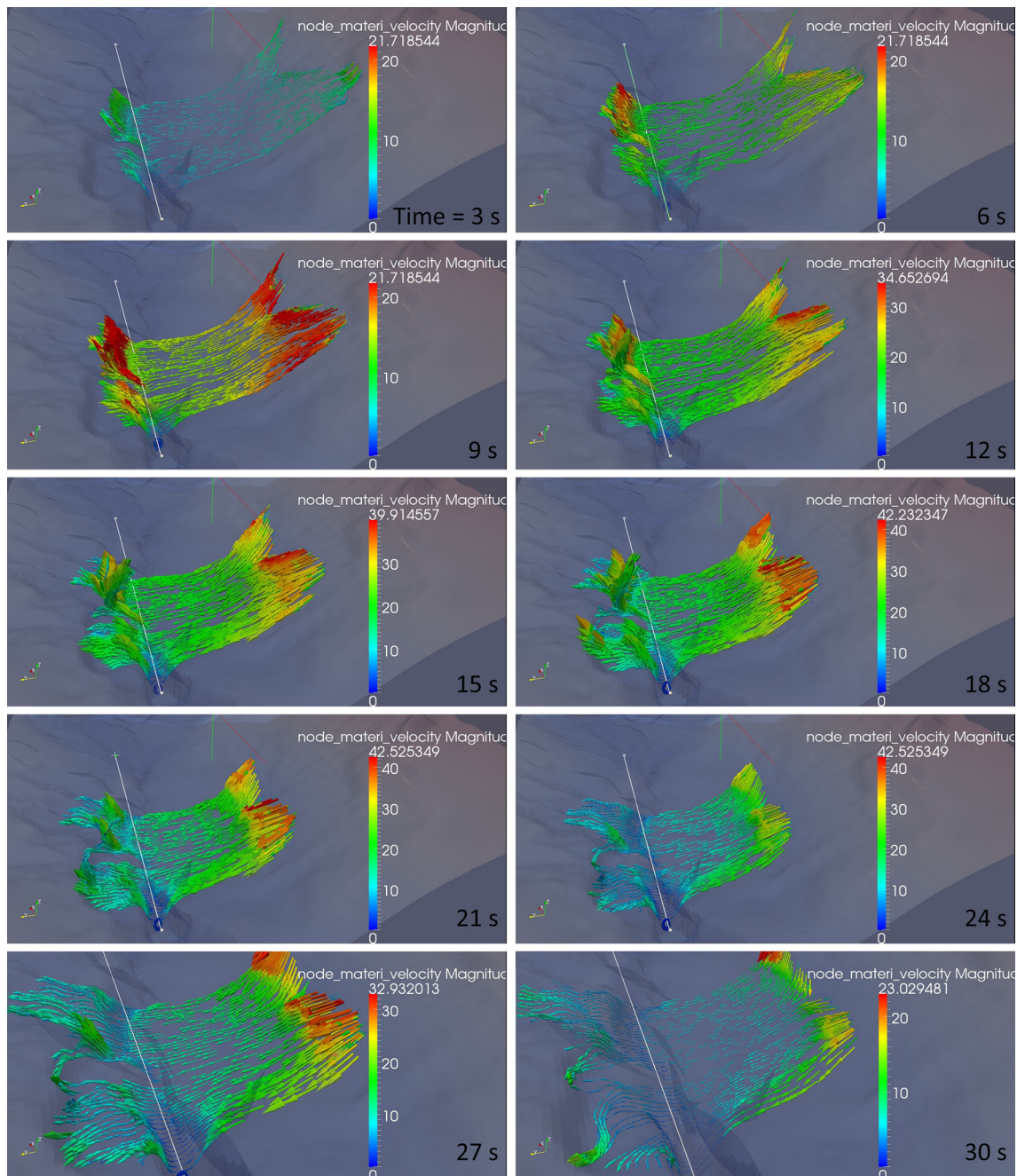


**Fig. 15** Results of the fully 3D simulation, showing the velocity vectors at different time steps (3-s interval). The colour scale changes to evidence the velocity distribution. Enlarged views are presented for the two last time steps

strong vertical and backward components causing an evident curl in the velocity vectors. After this stage the water wave collapses back on the surface and the subsequent evolution is controlled by flow along the slope and its local morphology, as well as by spreading upstream and downstream along the valley. The eastern and western masses forming the rockslide seem to have a similar behaviour and with some slight upstream and downstream movements

parallel to the valley. Generally, the maximum instantaneous front velocity remains between 20 and 30  $\text{m s}^{-1}$  with slightly higher values on the eastern sector and especially along the easternmost rockslide boundary.

In the latter phases (33–45 s), the westernmost sector of the rockslide, just above the dam, shows some material moving directly downstream of the dam within the left hand flank of the gorge. This difference with respect to



what has been observed after the event, as well as some differences in water wave maximum height, can result by the adopted discretization by 18-m high hexahedrons which can limit the resolution of the models.

Model validation was attained by comparing the final geometry of the rockslide deposit, the maximum water wave run-up limit (Fig. 15) and the duration of the different phases (i.e. rockslide motion and water wave generation). Figure 16 presents the results of such a comparison, whereas Fig. 17 compares the computed streamline geometry computed by the FE code for the rockslide and their real counterparts. The latter are represented by the relative displacement vectors of 49 well-recognizable points and rocky outcrops mapped by Rossi and Semenza (1986) before and after the collapse. The computed streamlines closely match the observed relative displacements further supporting the prediction capability of the model and of the numerical approach (Fig. 18).

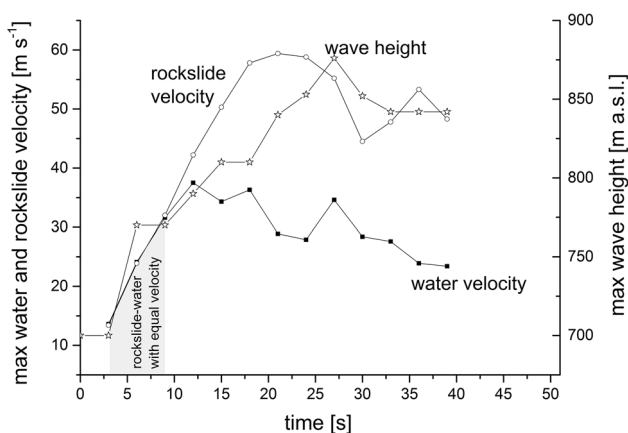


**Fig. 16** Plot of the maximum computed values of rockslide and water velocity and of water elevation computed by the fully 3D FEM ALE model. The grey area represents the time interval (3–9 s) during which rockslide and reservoir water move at very similar velocity

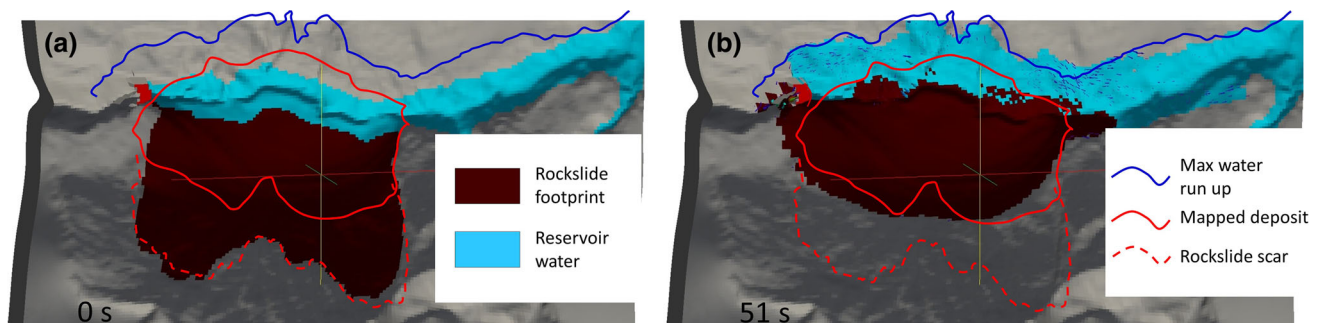


**Fig. 17** Comparison of the initial and final rockslide footprint (in brown) computed by the fully 3D simulation with respect to the post-failure boundaries (continuous red line) as mapped by Rossi and

## 4 Discussion

Various authors (Fritz et al. 2004; Heller and Kinnear 2010) observed and evaluated the relevance of different controlling variables on the generation of impulse waves, both in the near and the far field, and as a consequence also on the tsunami hazard assessment. Among these variables, we can list, namely profile of the sliding surface and its geometry at the transition between the sliding ramp and basin bottom, material properties, deformability, landslide length, landslide front shape, total front angle (i.e. sum of the angles of sliding surface and of the slide front; Heller and Spinneken 2013), landslide velocity and duration. Then, the rigidity of the impacting mass and consequently the slide geometry at the impact are extremely relevant to controlling the final results as well as the interaction with water or any other deformable material. Nevertheless, very few studies have tried and succeeded at simulating these ensemble of elements. On the contrary, some studies consider only an instantaneous change in the properties at the transition from subaerial to subaqueous conditions, but completely omit the impact at the water surface and the effects on the landslide (Table 1).

Using an FEM ALE code (Roddeman 2013), we performed a set of 2D and 3D simulations to verify its modelling capabilities. These included three extreme conditions observed in landslide-generated impulse waves, namely the Vajont rockslide, and the cases of an outward and backward collapsing hydrodynamic impact crater. These three different examples are characterized by different geometries and values of the slide Froude number: 0.25–0.9, 3.15 and 1.4. The Vajont case study is an extreme case where the water reservoir is much smaller than the slide, and due to the slide the reservoir bottom is raised during the motion and the water is swept away from its initial position.

It is worth mentioning that these results are obtained by using a reasonable set of average property values for the

Semenza (1965). **a** Initial reservoir geometry, **b** computed maximum water level rise compared with maximum wave run-up as mapped by Rossi and Semenza (1965)

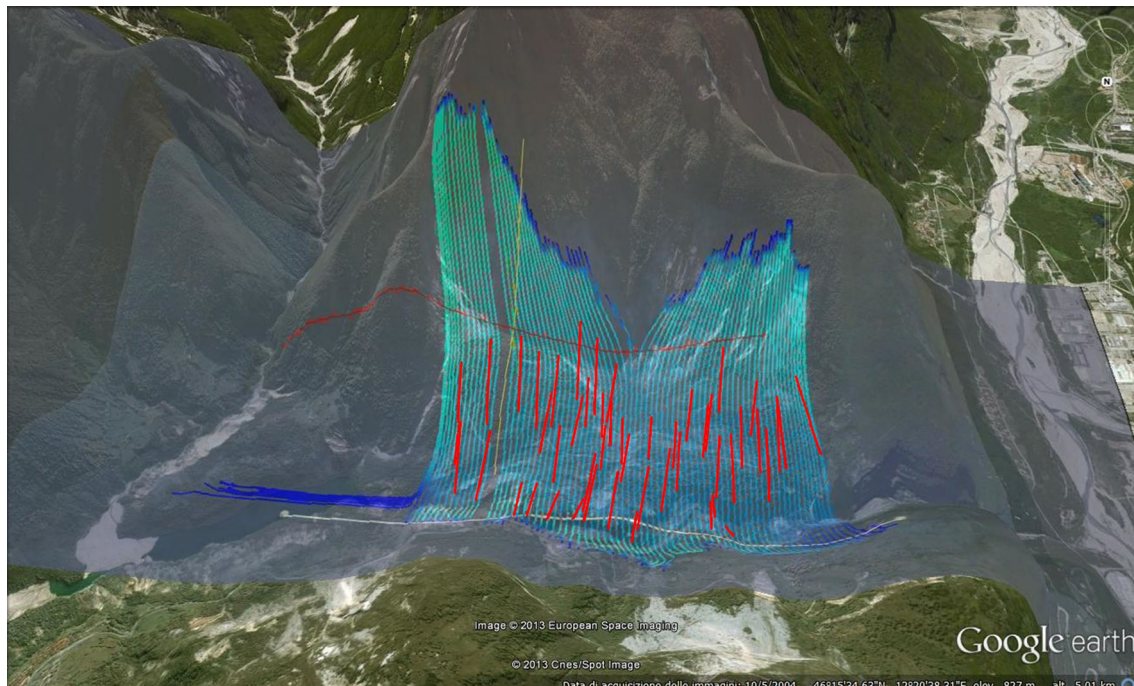


**Fig. 18** Comparison of the streamlines (long blue-coloured lines) computed by fully 3D FEM model with the relative displacement vectors (red lines) derived by linking the pre- and post-failure position of 49 recognizable geologic features from maps by Rossi and Semenza (1965)

**Table 1** Major historical landslide induced tsunamis with main relevant data and references

Location	Date	Landslide volume ( $10^6 \text{ m}^3$ )	Wave height (m)	Casualties	Reference
Langfjord, Norway	February 22nd, 1756	12	40	32	Blikra et al. (2005)
Mt. Ramnefjellet, Loen, Norway	January 15th, 1905	0.35	40	62	Blikra et al. (2005)
Mt. Ramnefjellet, Loen, Norway	September 13th, 1936	1	74	74	Blikra et al. (2005)
Tafjord, Norway	April 7th, 1934	1.5–3	62	44	Blikra et al. (2005)
Lituya Bay, Alaska	July 9th, 1958	30	524	5	Miller (1960)
Shimabara Bay, Japan	May 21st, 1792	535	10	15,000	Slingerland and Voight (1979)
Chungar collapse, Perù	March 18th, 1971	0.1	30	400–600	Plafker and Eyzaguirre (1979)
Pontesei Lake, Italy	March 22nd, 1959	3	33	1	Catenacci (1992); Semenza (2002); Panizzo et al. (2005b)
Vajont, Italy	October 9th, 1963	256	250	2000	Semenza (2002)
Val Pola, Italy	July 28th, 1987	50	35	27	Crosta et al. (2003)

rockslide material as determined from available laboratory tests and general rockslide descriptions. At the same time, some of the misfittings between models and experimental observations can be the result of some assumptions and simplifications, namely geometric approximations (DTM resolution), use of a “coarse” finite elements discretization (e.g. 3D fully deformable Vajont simulation with  $22 \text{ m} \times 22 \text{ m} \times 18 \text{ m}$  hexahedrons), approximation of

rigid boxes (Aknes rockslide model by Sælevik et al. 2009) with a slightly deformable mass, neglecting of water viscosity and material porosity and air inclusion. Nevertheless, the misfittings and differences seem to be contained within an acceptable range considering the uncertainties involved in some measurements and observations.

The 2D numerical results in the presence of the water reservoir roughly resemble the observations of the physical



model tests performed at Padua University (in 1968, see Datei 2003) with an equivalent time duration of 19 s using a 3- to 4-mm-sized gravel. In particular, the numerical model results in longer runout and larger run-up which can be easily explained by the slightly steeper failure surface and the lower basal friction angle as supported by the discovery of weak basal clayey layers.

In the presented set of 2D and 3D simulations for the Vajont rockslide, no water seepage is considered and the rockslide is always considered as impermeable. This seems reasonable considering its relatively short duration, the computed high velocities and the observed conditions of the rockslide front after the event. This point and its relevance have been pointed to and discussed by Erismann and Abele (2001), as mentioned previously. The same problem has been also partially discussed by Ghetti (1962) and other experimenters who used different types of granular materials to simulate the scaled rockslide.

This aspect of the modelling and its consequences on the runout and impulse wave run-up was also a major point in the paper presented by Zhao et al. (this issue), where DEM model using properties opportunely scaled for particles large enough to maintain a relatively low computational effort were used. A high hydraulic conductivity results from this assumption, but the approach includes also the saturation of the rockslide toe submerged below the initial reservoir level. This condition is quite similar to the one studied by Datei (2003) through experimental scaled models. The presence of a groundwater table and internal seepage can be also activated in FEM ALE models when this is considered relevant, in terms of effect of material hydraulic conductivity. At the same time, the models only consider the presence of one fluid (water) and exclude the possible effects related to the presence of air, which, in particular conditions, could play a role as for the case of a backward hydrodynamic crater collapse (Fritz et al. 2003b).

## 5 Conclusions

The study of the interaction between a rapidly moving landslide and a water reservoir is extremely interesting for the assessment of the associated level of hazard and risk. The relative characteristics of the water reservoir and of the landslide strongly influence the final result. In particular, the landslide and the wave evolution (initiation, propagation and run-up) are controlled by: initial landslide mass position (subaerial, partially or completely submerged), landslide speed, type of material, subaerial and subaqueous slope geometry, landslide depth and length at the impact, water depth and extent of the water body.

Therefore, the coupling of landslide modelling and water wave generation and propagation is fundamental and it has not been fully developed in past studies. In this paper, an FEM ALE approach is tested and adopted to simulate both 2D laboratory experiments and 3D rockslide evolution and impulse wave generation. The results of 2D water tank laboratory models published in the literature have been used to validate the numerical code capabilities at different landslide Froude numbers.

2D and fully 3D simulations have been presented for the Vajont rockslide runout and can be considered the first ones which couple a robust rockslide runout simulation with the generation of the impulse wave. To validate the numerical models, different aspects have been considered including, namely, total duration of the movement, maximum rockslide runout and water run-up, internal deformation, computed velocity and trajectories of marker points mapped before and after the event.

The same code was tested to simulate the interaction of rockslides and rock avalanches with erodible soil-like materials (Crosta et al. 2009, 2013a, b) showing its capabilities for catching various depositional features. Presently, the FEM ALE approach does not require a rescaling of the properties and of the particle size as in DEM and can include complex conditions which can become relevant in some special conditions (e.g. lower landslide velocity and large landslide hydraulic conductivity).

**Acknowledgments** This study has been partially funded by the EC Safeland Project, GA No.: 226479, Living with landslide risk in Europe: assessment, effects of global change, and risk management strategies. The research was partially funded by a MIUR-PRIN project: Time–Space prediction of high impact landslides under changing precipitation regimes. The Civil Protection Office of the Friuli Venezia Giulia Region is thanked for providing the ALTM-Lidar dataset of the Vajont valley. Monica Ghirotti and Michele Sapigni are thanked for their support and helpful discussions.

## References

- Abadie S, Morichon D, Grilli S, Glockner S (2010) Numerical simulation of waves generated by landslides using a multiple-fluid-Navier-Stokes model. *Coast Eng* 57:779–794
- Alonso EE, Pinyol NM (2010) Criteria for rapid sliding I. A review of Vajont case. *Eng Geol* 114(3):198–210
- Alonso EE, Pinyol NM, Puzrin AM (2010) Catastrophic slide: Vajont landslide, Italy. In: Alonso EE, Pinyol NM, Puzrin AM (eds) *Geomechanics of failures. Advanced topics*. Springer, The Netherlands, pp 33–81
- Ataie-Ashtiani B, Malek-Mohammadi S (2007) Near field amplitude of sub-aerial landslide generated waves in dam reservoirs. *Dam Eng* 17(4):197–222
- Ataie-Ashtiani B, Nik-Khah A (2008) Impulsive waves caused by subaerial landslides. *Environ Fluid Mech* 8(3):263–280
- Barla G, Antolini F, Barla M, Mensi E, Piovano G (2010) Monitoring of the Beauregard landslide (Aosta Valley, Italy) using advanced and conventional techniques. *Eng Geol* 116(3):218–235

- Belloni LG, Stefani R (1987) The Vajont slide: Instrumentation—Past experience and the modern approach. *Eng Geol* 24(1):445–474
- Blikra LH (2012) The Åknes rockslide, Norway. In: Clague JJ, Stead D (eds) *Landslides: types: mechanisms and modeling*. Cambridge University Press, Cambridge, pp 323–335
- Blikra L, Longva O, Harbitz C, Løvholt F (2005) Quantification of rock-avalanche and tsunami hazard in storfjorden, Western Norway. In: Flaate K, Larsen J, Senne set K (eds.) *Landslides and avalanches, ICFL 2005 Norway*. CRC press, pp 57–64
- Blikra LH, Longva O, Braathen A, Anda E, Dehls J, Stalsberg K (2006) Rock-slope failures in Norwegian fjord areas: examples, spatial distribution and temporal pattern. In: Evans SG, Scarascia Mugnozza G, Strom AL, Hermanns RL (eds) *Landslides from massive rock slope failure*. Nato Science Series IV, Earth and Environmental Sciences, 49, pp 475–496
- Boon CW, Houlsby GT, Utili S (2014) New insights in the 1963 Vajont slide using 2D and 3D distinct element method analyses. *Geotechnique* (in press). doi:10.1680/geot.14.P.041
- Bosa S, Petti M (2011) Shallow water numerical model of the wave generated by the Vajont landslide. *Environ Model Softw* 26(4):406–418
- Bosa S, Petti M (2013) A numerical model of the wave that overtopped the Vajont dam in 1963. *Water Resour Manage* 27(6):1763–1779
- Broili L (1967) New knowledge on the geomorphology of the Vajont slide slip surfaces. *Rock Mech Eng Geol J Int Soc Rock Mech* V(1):38–88
- Caloi P (1966) L'evento del Vajont nei suoi aspetti geodinamici. *Annali di Geofisica (Annals of Geophysics)* 1(19):1–74
- Calvino F, Gridel H, Roubault M, Stucky A (1967) Relazione dei periti nominate dal G.I. del tribunale di Belluno, in merito alla catastrofe del Vajont, del 9 ottobre 1963. Unpublished report
- Catenacci V (1992) Il dissesto geologico e geoambientale in Italia dal dopoguerra al 1990. Da Servizio Geologico Nazionale, Memorie descrittive della Carta Geologica d'Italia, Volume XLVII
- Chen WF, Han DJ (1988) *Plasticity for Structural Engineers*. Springer, New York, p 606
- Ciabatti M (1964) La dinamica della frana del Vajont. *Giornale di Geologia*, XXXII (1):139–154
- Crosta GB, Imposimato S, Roddeman D (2003) Modelling of landslide dynamics and generated water waves EAE03-A-14448; NH5-1FR4P-1777
- Crosta GB, Imposimato S, Roddeman DG (2006) Continuum numerical modelling of flow-like landslides. In: Evans SG, Scarascia Mugnozza G, Strom A, Hermanns R (eds) *NATO ARW, Landslides from massive rock slope failure*. NATO Science Series, Earth and Environmental Sciences, vol 49, pp 211–232
- Crosta GB, Frattini P, Imposimato S, Roddeman DG (2007) 2D and 3D numerical modeling of long runout landslides—the Vajont case study. In: Crosta GB, Frattini P (eds) *Landslides: from mapping to loss and risk estimation*. IUSS Press, Pavia, pp 15–24
- Crosta GB, Imposimato S, Roddeman DG (2008a) Approach to numerical modelling of long runout landslides. In: *Proceedings International forum on Landslide Disaster Management*, Hong Kong, GCO, 2007, p 20
- Crosta GB, Imposimato S, Roddeman DG (2008b) Numerical modelling of entrainment/deposition in rock and debris-avalanches. *Eng Geol* 109(1–2):135–145
- Crosta GB, Imposimato S, Roddeman D (2009) Numerical modeling of 2-D granular step collapse on erodible and nonerodible surface. *J Geophys Res* 114:F03020
- Crosta GB, Imposimato S, Roddeman D, Frattini P (2012) Landslide/reservoir interaction: 3D numerical modelling of the Vajont rockslide and generated water wave, vol 14, EGU2012-11908. Copernicus GmbH, Göttingen
- Crosta GB, Imposimato S, Roddeman D (2013) Interaction of landslide mass and water resulting in impulse waves. In: Margottini C, Canuti P, Sassa K (eds), *Landslide science and practice, vol 5 complex environment*. ISBN 978-3-642-31426-1, 28. doi:10.1007/978-3-642-31427-8. Springer Heidelberg, New York, pp 49–56
- Crosta GB, Imposimato S, Roddeman D, Frattini P (2013) On controls of flow-like landslide evolution by an erodible layer. In: Margottini C, Canuti P, Sassa K (eds) *Landslide science and practice, vol 3: spatial analysis and modelling*, ISBN 978-3-642-31426-1, 28. doi:10.1007/978-3-642-31427-8, Springer Heidelberg, New York, pp 263–270
- Cruden DM, Varnes D (1996) *Landslide types and processes*. In: Turner AK, Schuster RL (eds) *Landslides Investigation and Mitigation: Transportation Research Board Special Report 247*, National Research Council. National Academy Press, Washington, DC, pp 36–75
- Datei C (2003) *Vajont. La storia idraulica*. Libreria Internazionale Cortina, Padova, p 137, ISBN: 97888778425349, in Italian
- Davidson DD, McCartney BL (1975) Water waves generated by landslides in reservoirs. *J Hydraulics Div* 101(12):1489–1501
- Di Risio M, De Girolamo P, Beltrami GM (2011) Forecasting landslide generated tsunamis. In: Marner NA (ed) *Environmental sciences “The Tsunami threat—research and technology”*, InTech, ISBN 978-953-307-552-5, pp 81–106
- Enet F, Grilli ST (2007) Experimental study of tsunami generation by three-dimensional rigid underwater landslides. *J Waterw Port Coast Ocean Eng* 133(6):442–454
- Erismann TH, Abele G (2001) *Dynamics of rockslides and rockfalls*. Springer-Verlag, Berlin Heidelberg 328 pp
- Ferri F, Di Toro G, Hirose T, Han R, Noda H, Shimamoto T, de Rossi N (2011) Low-to-high-velocity frictional properties of the clay-rich gouges from the slipping zone of the 1963 Vajont slide, northern Italy. *J Geophys Res: Solid Earth* 116:B09208. doi:10.1029/2011JB008338
- Fritz HM (2002). Initial phase of landslide generated impulse waves. Thesis Versuchsanstalt für Wasserbau, Hydrologie und Glaziologie, ETH Zürich, Swiss ETH No. 14'871. Swiss Federal Inst. Techn., Zürich, ISSN 0374-0056
- Fritz HM, Hager WH, Minor H-E (2001) Lituya Bay case: rockslide impact and wave run-up. *Sci Tsunami Hazards* 19(1):3–22
- Fritz HM, Hager WH, Minor H-E (2003a) Landslide generated impulse waves 1. Instantaneous flow fields. *Exp Fluids* 35:505–519
- Fritz HM, Hager WH, Minor H-E (2003b) Landslide generated impulse waves 2. Hydrodynamic impact craters. *Exp. Fluids* 35:520–532
- Fritz HM, Hager WH, Minor H-E (2004) Near field characteristics of landslide generated impulse waves. *J. Waterw. Port Coastal Ocean Eng*. 130(6):287–302
- Fritz HM, Mohammed F, Yoo J (2009) Lituya Bay landslide impact generated mega-tsunami 50th anniversary. *Pure Appl Geophys* 166(1–2):153–175
- Ghetti A (1962) *Esame sul modello degli effetti di un'eventuale frana el Lago – Serbatoio del Vajont*. S.A.D.E. Venezia, Centro Modelli Idraulici E. Scimeni, Ricerca n. 10, p 23
- Ghirotti, M. (2012) The 1963 Vajont landslide, Italy. In: JJ Clague, Stead D (eds) *Landslides: types, mechanisms and Modeling*. Cambridge University Press, pp 359–372
- Grilli ST, Watts P (2005) Tsunami generation by submarine mass failure Part I: modeling, experimental validation, and sensitivity analysis. *J Waterw Port Coast Ocean Eng* 131(6):283–297
- Grilli ST, Vogelmann S, Watts P (2002) Development of a 3D numerical wave tank for modeling tsunami generation by underwater landslides. *Eng Anal Bound Elem* 26(4):301–313

- Harbitz CB (1992) Model simulations of tsunamis generated by the Storegga slides. *Mar Geol* 105:1–21
- Harbitz CB, Glimsdal S, Løvholt F, Kveldsvik V, Pedersen G, Jensen A (2014) Rockslide tsunamis in complex fjords: From an unstable rock slope at Åkerneset to tsunami risk in western Norway. *Coast Eng* 88:101–122. doi:10.1016/j.coastaleng.2014.02.003
- Heller V (2007) Landslide generated impulse waves: Prediction of near field characteristics. Thesis, ETH Zürich, Swiss ETH No. 17531. Swiss Federal Inst. Techn., Zürich
- Heller V, Hager WH (2010) Impulse product parameter in landslide generated impulse waves. *J Waterw Port Coast Ocean Eng* 136(3):145–155
- Heller V, Kinnear RD (2010) Discussion of “Experimental investigation of impact generated tsunamis; related to a potential rock slide, Western Norway” by G. Sælevik, A. Jensen, G. Pedersen [*Coastal Eng.* 56 (2009) 897–906]. *Coast Eng* 57(8):773–777
- Heller V, Spinneken J (2013) Improved landslide-tsunami prediction: Effects of block model parameters and slide model. *J Geophys Res Ocean* 118:1489–1507. doi:10.1002/jgrc.20099
- Hendron AJ, Patton FD (1985) The Vaiont slide, a geotechnical analysis based on new geological observations of the failure surface. Tech Rep GL-85-5, vol 2 Department of the Army, US Corps of Engineers, Washington, DC
- Huber A (1980) Schwallwellen in seen als floger von felsstürzen (reservoir impulse waves caused by rockfall), Technical Report Mitteilung 47, Lab. Hydraulics, Hydrology and Glaciology, ETH
- Huber A, Hager WH (1997) Forecasting impulse waves in reservoirs, Commission Internationale des Grands Barrages, 19th Congress des Grand Barrages. Florence 1997:993–1005
- Hunter SC (1983) *Mechanics of Continuous Media*, 2nd edn. Ellis Horwood, Chichester, p 640
- Ischuk AR (2011) Usoi Rockslide Dam and Lake Sarez, Pamir Mountains, Tajikistan. In: Evans SG, Hermanns RL, Strom A, Scarascia-Mugnozza G (eds) *Natural and artificial rockslide dams*. Springer, Heidelberg, pp 423–440
- Jiang L, LeBlond PH (1993) Numerical modeling of an underwater Bingham plastic mudslide and the wave which it generates. *J Geophys Res* 98:304–317
- Jørstad F (1968) Waves generated by landslides in Norwegian Fjords and Lakes. Norwegian Geotechnical Institute publication, Norway, p 79
- Kalenchuk KS, Hutchinson DJ, Diederichs M, Moore D (2012) Downie slide, British Columbia, Canada. In: Clague JJ, Stead D (eds) *Landslides: types mechanisms and modeling*. Cambridge University Press, Cambridge, pp 345–357
- Kamphuis JW, Bowering RJ (1970) Impulse waves generated by landslide, Proceedings of 12th coastal engineering conference, pp 575–588
- Keating BH, McGuire WJ (2000) Island edifice failures and associated tsunami hazards. *Pure appl Geophys* 157:899–955
- Larsen JO (ed) *Landslides and avalanches*. In: Proceedings of the 11th international conference and field trip on landslides, Norway, 1–10 September 2005. Taylor & Francis Group, London, pp 57–63
- Liao H, Ying J, Gao S, Sheng Q (2005) Numerical analysis on slope stability under variations of reservoir water level. In: Sassa K, Fukuoka H, Wang F, Wang G (eds) *Landslides. Risk analysis and sustainable disaster management*. Proceedings 1st general assembly int. cons. on landslides, Springer, 304–311
- Lynett P, Liu PLF (2005). A numerical study of the run-up generated by three-dimensional landslides. *J Geophys Res* 110 C03006:16 doi:10.1029/2004JC002443
- Macfarlane DF (2009) Observations and predictions of the behaviour of large, slowmoving landslides in schist, Clyde Dam reservoir, New Zealand. *Eng Geol* 109:5–15
- Miller D (1960) Giant waves in Lituya Bay Alaska. USGS Prof. Paper, 354-C, pp 51–83
- Müller L (1964) The rock slide in the Vaiont valley. *Rock Mech Eng Geol* 2(3/4):148–212
- Müller D (1995). Auflaufen und überschwappen von impulswellen an talsperren (run-up and overtopping of impulse waves at dams), Technical Report Mitteilung 137, Lab. of Hydraulics, Hydrology and Glaciology, ETH
- Noda E (1970) Water waves generated by landslides. *J Waterw Harb Coast Eng Div ASCE* 96 (WW4):835–855
- Panizzo A, De Girolamo P, Petaccia A (2005a) Forecasting impulse waves generated by subaerial landslides. *J Geophys Res Ocean* (1978–2012), 110(C12)
- Panizzo A, De Girolamo P, Di Risio M, Maistri A, Petaccia A (2005b) Great landslide events in Italian artificial reservoirs. *Nat Hazard Earth Syst Sci* 5:733–740
- Pastor M, Herreros I, Fernández Merodo JA, Mira P, Haddad B, Quecedo M, González E, Alvarez-Cedron C, Dremptic V (2009) Modelling of fast catastrophic landslides and impulse waves induced by them in fjords, lakes, and reservoirs. *Eng Geol* 109:124–134
- Pinyol NM, Alonso EE (2010) Criteria for rapid sliding II.: thermo-hydro-mechanical and scale effects in Vaiont case. *Eng Geol* 114(3):211–227
- Plafker G, Eyzaguirre VR (1979) Rock avalanche and wave at Chungar, Peru. In: Voight B (ed) *Rockslides and avalanches*, vol 2. Developments in Geotechnical Engineering, vol 14B, Elsevier, Amsterdam, the Netherlands, 269–279
- Quecedo M, Pastor M, Herreros MI (2004) Numerical modelling of impulse wave generated by fast landslides. *Int J Numer Methods Eng* 59:1633–1656
- Roddean DG (2013) TOCHNOG user’s manual. FEAT, p 255, [www.feat.nl/manuals/user/user.html](http://www.feat.nl/manuals/user/user.html)
- Rossi D, Semenza E (1965) Carte geologiche del versante settentrionale del M. Toc e zone limitrofe, prima e dopo il fenomeno di scivolamento del 9 ottobre 1963, Scala 1:5000, Ist. Geologia Università di Ferrara, 2 Maps
- Rossi D, Semenza E (1986) Carta geologica del versante settentrionale del M. Toc e zone limitrofe. In: Masè G, Semenza M, Semenza P, Semenza P, Turrini MC, 2004, Le foto della frana del Vajont. [http://www.k-flash.it/editoria\\_en.html](http://www.k-flash.it/editoria_en.html)
- Roubault M. (1967) Esperienze su un modello della Valle del Vaiont. In Calvino et al. (1967), unpublished report
- Sælevik G, Jensen A, Pedersen G (2009) Experimental investigation of impact generated tsunamis; related to a potential rock slide, Western Norway. *Coast Eng* 56(9):897–906
- Selli R, Trevisan G (1964) La frana del Vaiont. *Annali Mus Geol Serie* 2(32):1
- Semenza E (1965) Sintesi degli studi geologici sulla frana del Vaiont dal 1959 al 1964. *Mem Mus Trident Sci Nat*, A XXIX–XXX (16), pp 1–51
- Semenza E (2002) La storia del Vajont. Tecnoproject, Ferrara, p 280 (in Italian)
- Semenza E (2010) The story of Vajont told by the geologist who discovered the landslide. k-flash Ed, Ferrara, p 205. Available at [www.k-flash.it](http://www.k-flash.it)
- Semenza E, Ghirotti M (2000) History of 1963 Vaiont Slide. The importance of the geological factors to recognise the ancient landslide. *Bull Eng Geol Env* 59:87–97
- Sitar N, MacLaughlin MM, Doolin DM (2005) Influence of kinematics on landslide mobility and failure mode. *J Geotech Geoenviron Eng* 131(6):716–728
- Skempton AW (1966) Bedding-plane slip, residual strength and the Vaiont Landslide. *Géotechnique* XVI(1):82–84
- Slingerland RL, Voight B (1979) Occurrences, properties, and predict models of landslide-generated water waves. In: Voight B (ed)

- Rockslides and avalanches 2, vol 14B. Elsevier, Developments in Geotechnical Engineering, Amsterdam, pp 317–397
- Sosio R, Crosta GB, Hungr O (2012) Numerical modeling of debris avalanche propagation from collapse of volcanic edifices. *Landslides* 9(3):315–334
- Sue LP, Nokes RI, Walters RA (2006) Experimental modelling of tsunami generated by underwater landslides. *Sci Tsunami Hazards* 24(4):267–287
- Superchi L (2012) The Vajont rockslide: new techniques and traditional methods to re-evaluate the catastrophic event. PhD Thesis, Padova University, p 215
- Tika ThE, Hutchinson JN (1999) Ring shear tests on soil from the Vaiont landslide slip surface. *Geotechnique* 49(1):59–74
- Vacondio R, Mignosa P, Pagani S (2013) 3D SPH numerical simulation of the wave generated by the Vajont rockslide. *Adv Water Resour* 59:146–156
- Vardoulakis I (2000) Catastrophic landslides due to frictional heating of the failure plane. *Mech Cohes Frict Mater* 5:443–467
- Varnes DJ (1978) Slope movement types and processes. Transportation research board special report (176)
- Veveakis E, Vardoulakis I, Di Toro G (2007) Thermoporoelasticity of creeping landslides: the 1963 Vaiont slide, northern Italy. *J Geophys Res: Earth Surf* 112:F03026. doi:[10.1029/2006JF000702](https://doi.org/10.1029/2006JF000702)
- Viparelli M, Merla G (1968). L'onda di piena seguita alla frana del Vajont. Università degli Studi di Napoli (in Italian)
- Viroulet S, Cébron D, Kimmoun O, Kharif C (2013) Shallow water waves generated by subaerial solid landslides. *Geophys J Int* 193:747–762
- Votruba L (1966) L'éboulement de la pente gauche dans le lac-reservoir du Vajont. Expert report
- Wang F, Li T (2009) Landslide disaster mitigation in Three Gorges reservoir. Environmental Science and Engineering, Springer, China, p 563
- Wang F, Wang G, Sassa K, Takeuchi A, Araiba K, Zhang Y, Peng X (2005) Displacement monitoring and physical exploration on the Shuping Landslide reactivated by impoundment of the Three Gorges Reservoir, China. In: Sassa K, Fukuoka H, Wang F, Wang G (eds) Landslides. Risk analysis and sustainable disaster management. Proceedings 1st general assembly int consortium on landslides, Springer, pp 313–319
- Wang F, Zhang Y, Huo Z, Peng X, Wang S, Yamasaki S (2008) Mechanism for the rapid motion of the Qianjiangping landslide during reactivation by the first impoundment of the Three Gorges Dam reservoir China. *Landslides* 5(4):379–386
- Ward SN, Day S (2003) Ritter Island Volcano—lateral collapse and the tsunami of 1888. *Geophys J Int* 154:891–902
- Ward SN, Day S (2011) The 1963 landslide and flood at Vaiont Reservoir Italy. A tsunami ball simulation. *Ital J Geosci* 130(1):16–26
- Watts P (1998) Wavemaker curves for tsunamis generated by underwater landslides. *J Waterw Port Coast Ocean Eng* 124(3):127–137
- Watts P (2000) Tsunami features of solid block underwater landslides. *J Waterw Port Coast Ocean Eng* 126(3):144–152
- Wiegel RL, Noda EK, Kuba EM, Gee DM, Tornberg GF (1970) Water waves generated by landslide in reservoirs. *J Waterw Harb Coast Eng Div ASCE* 96 (WW2):307–333
- Zangerl C, Eberhardt E, Perzmaier S (2010) Kinematic behaviour and velocity characteristics of a complex deep-seated crystalline rockslide system in relation to its interaction with a dam reservoir. *Eng Geol* 112(1):53–67
- Zaniboni F, Tinti S (2014) Numerical simulations of the 1963 Vajont landslide, Italy: application of 1D Lagrangian modelling. *Nat Hazards* 70(1):567–592
- Zhang D, Wang G, Yang T, Zhang M, Chen S, Zhang F (2013) Satellite remote sensing-based detection of the deformation of a reservoir bank slope in Laxiwa Hydropower Station, China. *Landslides* 10:231–238. doi:[10.1007/s10346-012-0378-9](https://doi.org/10.1007/s10346-012-0378-9)
- Zhao T, Uthi S, Crosta GB (2014) Rockslide and impulse wave modelling in the Vajont reservoir by DEM-CFD analyses. Rock mechanics, Springer
- Zweifel A (2004) Impulswellen: Effekte der Rutschdichte und der Wassertiefe. PhD thesis, ETH Zurich, Zurich